KIMIKA FAKULTATEA
FACULTAD DE QUÍMICA

Basque Country University /Universidad del País Vasco

Faculty of Chemistry / Facultad de Ciencias Químicas

Chemistry degree

FINAL DEGREE THESIS

Organic-inorganic hybrid thermoelectric materials by a concept of simultaneous vapor phase infiltration (VPI/SCIP) of polymers by Bi_2S_3

Author: Raquel Corredor Conde

Directed by: Mato Knez
Txema Mercero

September of 2022, San Sebastián

GIPUZKOAKO CAMPUSA
CAMPUS DE GIPUZKOA
Pº. Manuel de Lardizabal, 3
20018 DONOSTIA-SAN SEBASTIAN
GIPUZKOA

This final degree thesis has been performed at:

CIC nanoGUNE

Nanomaterials group

Donostia-San Sebastián, SPAIN

ABSTRACT

The aim of the present work is to design new hybrid thermoelectric (TE) materials by vapor phase infiltration (VPI). VPI is a process which derives from atomic layer deposition (ALD) and bases on the same instrumental setup. However, it is not applied to solid substrates but to polymeric substrates, which causes that the precursors not only bind to the surface, but also diffuse into the polymer through vapor– solid dissolution. Upon diffusion and binding an inorganic–organic hybrid material is generated inside the bulk of the polymer. The extension of the infiltrated area into the bulk of the polymer can be modified by changing the exposure times, but it also can vary in dependence on the diffusivity of the precursors inside the polymer. Therefore, it is dependent on both the polymer and precursor characteristics. These key differences make VPI for the fabrication of new hybrid materials. In the present work we created such a new hybrid material set with covalently bound organic/inorganic interfaces by hybridization of the inorganic TE material Bi_2S_3 with the semiconducting polymers PEDOT: PSS and PANI. The hybridization process was monitored *in-situ* with a Quartz Crystal Microbalance (QCM). The monitoring allowed studying the VPI process in detail and quantitatively controlling the loading of inorganic precursors like $BiCl_3$ and H_2S into polymers bulk, thus allowing an extra degree of flexibility for tuning the material properties. The chemical composition and structure of the resulting hybrid materials upon various stages of infiltration was analyzed with high resolution transmission electron microscopy (HRTEM) and energy dispersive X-ray spectroscopy (EDX). The results showed that VPI provides a high degree of control on the inorganic phase distribution and overall composition of the hybrids by tuning the process parameters such as temperature, penetrant pressure, and exposure time. The obtained results offer new solutions for the waste-heat-to-energy industry.

RESUMEN

Este trabajo tiene como objetivo diseñar nuevos materiales termoeléctricos (TE) híbridos mediante infiltración en fase vapor (VPI). El origen del VPI reside en la técnica de deposición de capas atómicas o ALD y se basa en el mismo montaje instrumental. Sin embargo, no se aplica a sustratos sólidos sino a sustratos poliméricos, lo que hace que los precursores no sólo se unan a la superficie como en el caso del ALD, sino que también se difundan en el polímero a través de la disolución vapor-sólido. Tras la difusión y la unión, se genera un material híbrido inorgánico-orgánico dentro del polímero. La extensión del área infiltrada en la masa del polímero puede modificarse cambiando los tiempos de exposición, además de poder variar también en función de la difusividad de los precursores dentro del polímero. Por lo que depende tanto de las características del polímero como del precursor. Estas diferencias clave hacen que el VPI sirva para la fabricación de nuevos materiales híbridos. En el presente trabajo hemos creado un nuevo conjunto de materiales híbridos con interfaces orgánicas/inorgánicas unidas covalentemente mediante la hibridación del material inorgánico TE Bi_2S_3 con los polímeros semiconductores PEDOT: PSS y PANI. El proceso de hibridación se monitorizó *in-situ* con una microbalanza de cristal de cuarzo (QCM). La monitorización permitió estudiar el proceso de VPI en detalle y controlar cuantitativamente la carga de precursores inorgánicos como el $BiCl_3$ y el H_2S en los polímeros, permitiendo así un grado extra de flexibilidad para la mejora de las propiedades del material. La composición química y la estructura de los materiales híbridos resultantes tras varias etapas de infiltración se analizaron con microscopía electrónica de transmisión de alta resolución (HRTEM) y espectroscopia de rayos X de dispersión de energía (EDX). Los resultados mostraron que el VPI proporciona un alto grado de control sobre la distribución de las fases inorgánicas y la composición general de los híbridos mediante el ajuste de los parámetros del proceso, como la temperatura, la presión del penetrante y el tiempo de exposición. Los resultados obtenidos en esta tesis ofrecen nuevas soluciones para la industria de conversión de residuos en energía.

CONTENTS

1. INTRODUCTION

1.1. Background

In recent years, energy consumption and environmental pollution have grown exponentially which generated the urgent demand for clean and renewable energy sources, which ideally also reduce energy losses. Reducing greenhouse gas emissions is one of the key aspects to reduce the impact on the environment. In 2009, the European Union (EU) committed to reduce greenhouse gas (GHG) emissions by 80–95% from 1990 levels by 2050. Consequently, three roadmaps have been launched for this purpose: the "Roadmap for Moving to a Competitive Low Carbon Economy in 2050", the "Roadmap to a Single European Transport Area — Towards a Competitive and Resource Efficient Transport System" and the "Energy Roadmap 2050". [1]

One strategy to reduce greenhouse gas emissions and therefore increase energy efficiency is to capture and recycle the "waste" heat from all energy conversion processes. Approximately 30 to 40% of all heat is recovered and reused while the rest, such as 60-70% in automobiles, is lost as waste heat through the coolant or the exhaust. [2] Moreover, to convert thermal energy into electrical energy thermoelectric generators (TEGs) are used which operate with thermoelectric materials (TEs), a special class of materials that allow such heat to electricity conversion. The efficiency mainly depends on the dimensionless so-called thermoelectric ¨figure of merit¨ (FoM), ZT, shown in equation 1:

$$ZT = \frac{S^2 \cdot \sigma \cdot T}{k_{total}} \quad \textbf{(1)}$$

It is composed by S, the Seebeck coefficient (magnitude of an induced voltage resulting from a thermal gradient across a material), σ, the electrical conductivity, k_{total},the thermal conductivity with its lattice and electronic components ($k_{total} = k_e + k_{lat}$, being k_e electron-hole transportation and k_{lat} phonons travelling through the lattice), and T, the working temperature. To obtain optimal TE materials with a high electrical conductivity, a high ZT is needed. For this aim, according to the FoM equation, a large S value for high voltage output and a large σ to reduce Joule heating are needed. Moreover, a low k value is also needed to maintain a large temperature gradient. [3] This is a complex task for researchers because of the high dependency of these properties on each other.

Considerable attention has been paid to inorganic thermoelectric materials because of their typically high S and σ values. However, their high cost and low efficiency triggered the search for alternatives. Organic materials are cheap, have a low density and thermal conductivity, but they haven´t been investigated in depth for their low FoM value, which is usually 2-3 orders of magnitude lower than that of inorganic materials. This is explained by the low S, σ and power factor. In the case of organics, ZT reaches a value of 0.42 at room temperature, while inorganics can get up to 2.2 at temperatures over 900 K, being in this way, not efficient. [4] As a result, the combination of both materials to hybrid thermoelectric materials with high S and high σ of inorganic materials and low thermal conductivity of the organic materials has been recently very much demanded. There are different methods to improve the TE efficiency of hybrid materials, including controlling the inorganic nanostructure, modifying the organic materials, and engineering the interfaces within the material. [5]

Polymers were considered electrically insulating until Shirakawa et al. [6] discovered that polyacetylene can get relatively high electrical conductivities. Their thermal conductivity is normally 1 order lower than that of inorganic TEs. Consequently, polyaniline (PANI), polypyrrole (PPy) and poly(3,4-ethylenedioxythiophene):poly(styrenesulfonate) (PEDOT:PSS) are good candidates for exploring new TEs.

In 2018, flexible organic-inorganic hybrids with dispersed nanoparticles of Bi_2Te_3 in conductive PEDOT:PSS were reported by Wang et al. [7] The particles dispersed the phonons while the polymer provided the electronic transportation, achieving a ZT of 0.58 at 300K. Moreover, Fan et al. [8] informed how to improve the TE properties of the PEDOT:PSS by ion accumulation of the ionic liquid in the surface of the polymer. By this technique, the obtained result for the ZT had a value of 0.75 at 300 K. The obtained numbers were the two highest values of ZT reported for bulk polymers. Higher values of ZT (ZT>1) were found for ethylenedioxythiophene (EDOT) molecular wires doped with toluene sulfonate, resulting in an increasing of the S and s and in a decreasing of κk, obtaining a ZT of 2.4.

The main disadvantage of structures such as nanowires and nanorods is the difficulty to contact them. Even so, the hybrid TE materials currently available have some limitations: firstly, the physical interactions between inorganic and organic phases reduce the long-term stability and restrict the carrier transport in this kind of materials, and secondly, the limited control of the inorganic and organic phases at the nanoscale make the controlled and enhanced dispersion of the phonons in those materials difficult. To further develop these materials and overcome the

challenges presented by them, this thesis explores new hybrid TE materials by the application of vapor phase infiltration (VPI) of inorganic precursors into polymers.

1.2. Atomic Layer Deposition (ALD)

Atomic layer deposition (ALD) is a thin film deposition technique based on the sequential, self-limiting reactant exposure steps. It allows to deposit various conformal and highly uniform inorganic thin films on surfaces with a (sub-)monolayer precision. This technique was initially referred as atomic layer epitaxy (ALE) until approximately the 2000s, when the term "ALD" started to be used. ALE was developed in Finland by the pioneer Tuomo Suntola in the 1970s who created ZnS thin-film electroluminescent (TFEL) displays that were operated in the airport of Helsinki between 1983 and 1998. Since most of the films developed in the following years did not grow epitaxially, a renaming from the ALE to the ALD occurred and nowadays, this last naming dominates, while ALE nowadays stands for atomic layer etching, a process opposite to ALD. Semiconductor processing, deposition of high-quality dielectrics to produce trench capacitors for DRAM, low electron leakage dielectrics for magnetic read/write heads have been the main uses of the ALD in the recent years. Moreover, other applications have been developed because of the need to coat high aspect ratio structures, which are necessary for the miniaturization in the semiconductor industry, conformally. [9]

This process consists of two vaporized precursors where one of them is a metal source, such as an organometallic precursor, and another acts as oxygen or nitrogen source, for example, H_2O and NH_3. The precursors are supplied to the reactor in alternate vapor pulses. To obtain a conformal completion, the precursors will react with the terminal surface of the substrate and desorb from the parts where the precursor is already adsorbed until the surface is fully covered. To obtain a self-limiting process, there must not be any reaction between the two precursors in the gas-phase, but only on the surface. This can be obtained by purging the reactor with an inert gas as nitrogen between the individual pulses, which will result in a monolayer coating on the surface. Choosing the right type of substrate is crucial due to the different behaviors they can show at the end of the process. For example, solid inorganic substrates are selected in most cases due to their capacity to promote the coating process up because of the higher concentration of surface functional groups and reactivity to bind the vaporized precursors rapidly and efficiently. Otherwise, if soft materials (e.g. polymers) are chosen, the precursor can

diffuse into the substrate, resulting in a subsurface growth of the inorganic material. This will often provide some completely different properties to the polymer. [10]

Experimentally, the most studied ALD process is the trimethylaluminum (TMA)-water system because of the ideally self-terminating nature of the chemisorption and inertness of the reaction with methane as a byproduct. Aluminum oxide, Al_2O_3, is an important dielectric material used in a variety of applications such as protective coating or flat-screen electroluminescent displays and is mainly deposited using TMA and water precursors as depicted in Figure 1. Reaction 1 is the full reaction of TMA and water, while reactions 2 and 3 show the intermediate steps upon TMA-pulse and water-pulse, respectively. [11]

$$Al(CH_3)_3 + {}^3/_2\ H_2O \rightarrow {}^1/_2\ Al_2O_3 + 3CH_4 \qquad \textbf{Reaction 1}$$

$$II\text{-}OH + Al(CH_3)_3 \rightarrow II\text{-}O\text{-}Al(CH_3)_2 + CH_4 \qquad \textbf{Reaction 2}$$

$$II\text{-}O\text{-}Al(CH_3)_2 + H_2O \rightarrow II\text{-}O\text{-}Al(CH_3)OH + CH_4 \qquad \textbf{Reaction 3}$$

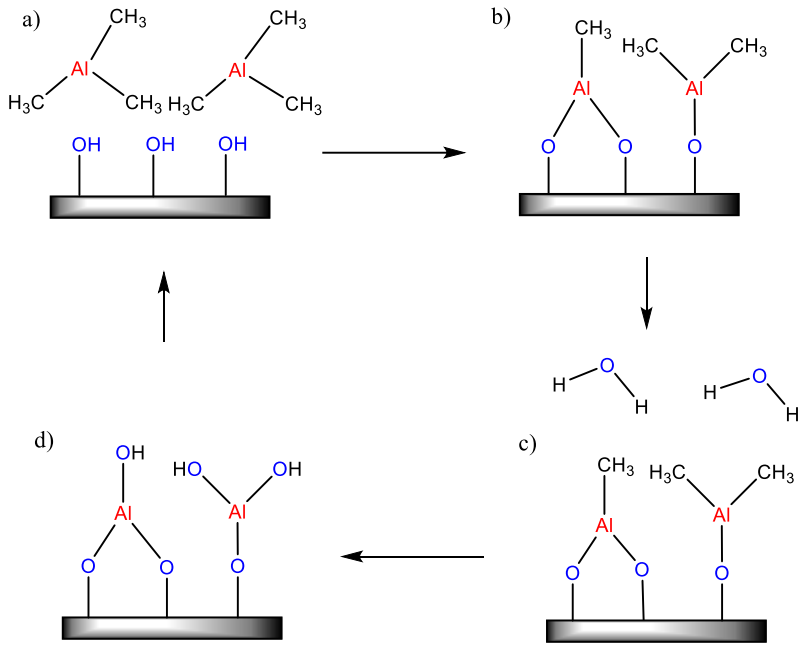

***Figure 1**. Schematic representation of the surface reactions for the growth of a substrate monolayer with TMA-H_2O as precursors. (a) TMA adsorption to the substrate surface, (b) purge the TMA vapor out of the reaction chamber, (c) water reacts with the saturated surface, (d) H_2O is flushed out from the system.*

The mechanism of one cycle as it is shown in figure 1 consists firstly of the chemisorption of TMA on the substrate surface. After this, methyl groups from TMA form a methane molecule with the proton of the hydroxyl group which desorbs into the gas phase. Once the TMA has saturated the surface, the gas-phase is purged with an inert gas such as nitrogen and followed by water pulse that reacts with the adsorbed TMA removing the remaining methyl groups and hydroxylates the surface for the following TMA pulse finishing this cycle with a monolayer of Al_2O_3.

Throughout the ALD process, there is a temperature range where the ALD behaves almost ideally. The so-called "ALD-window" depicts a temperature zone in which a controlled film proceeds (Figure 2).

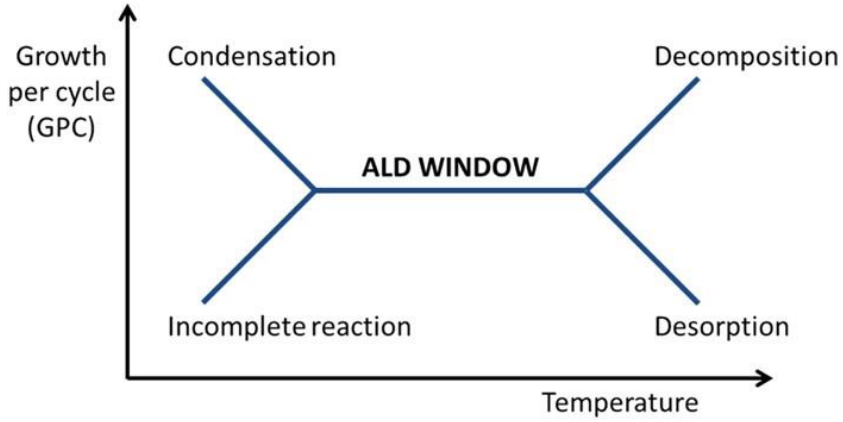

Figure 2. *ALD window representation indicating the growth per cycle as function of the deposition temperature.* [12]

Outside the temperature window, at lower or higher temperatures, non-self-limiting and uncontrolled growth occurs. On one hand, at lower temperatures, surface reactions may be incomplete because of the lack of thermal energy leading to a decreased growth per cycle, or the precursor could condense on the surface giving a more rapid growth per cycle as result. On the other hand, at high temperatures, the precursor from the substrate could desorb, reducing the growth or thermal decomposition of the precursor (chemical vapor deposition (CVD)) can result in an increase growth per cycle. [9]

1.3. Vapor Phase Infiltration (VPI)

Vapor phase infiltration (VPI) derives from ALD. Both techniques are based on the same strategy and technology, but VPI allows the precursors not only to grow on the top of the substrate surface as in the case of ALD, but also to diffuse into a polymeric substrate through a vapor solid

dissolution process, generating an inorganic–organic hybrid material in the subsurface area of the polymer. In figure 3, the schematic depicts differences of the process results. On the left hand side a coating results from the ALD process, where thin films are deposited on the surface of the substrate by sequential doses of multiple (two or more) vaporized precursors, creating a coating on the surface. On the right hand side, the VPI technique generates a final hybrid material with the top coating and the chemically modified subsurface of the polymer.

***Figure 3**. Schematic of the comparison between samples processed by ALD (left) and VPI (right).*

For this aim, between the precursor pulse and purge, an exposure step is introduced to provide sufficient time for the precursor vapor to diffuse into the polymer bulk and form crosslinks after reacting with the polymer functional groups, which allows the formation of a unique hybrid material. The completion of the VPI sequence cycle occurs by a counter-reactant pulse. The second gas phase reaction takes place between the initially infiltrated reactive species and the second precursor, hydrolyzing, oxidizing or reducing the initial precursor.

The penetration depth and density of the inorganic fraction into the polymer can change with the number of cycles, exposure time or other parameters like the processing temperature.

The combination of ALD and VPI processes is called simultaneous vapor phase coating and infiltration process (SCIP), allows to coat and infiltrate the polymer substrate with two distinct or equal materials in the same run. [13] SCIP ensures benefits over the individual ALD and VPI and provides a good separation of the two different materials and therefore, can offer different advantages as the simplicity of the processing for example creating hybrid materials and the increase of time saved in each cycle. In figure 4, an example of the material´s hierarchy after VPI and SCIP with a hybrid layer and inorganic coating on top of the polymer substrate is schematized. This allows to obtain bi- or multilayers with completely different properties within one material.

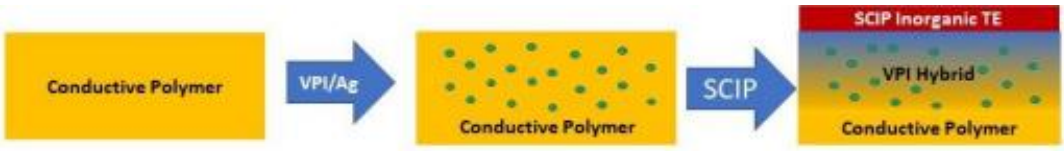

Figure 4. *Schematic of material´s hierarchy after VPI (blue) and SCIP (red) with created hybrid layer and inorganic coating on top of the polymer substrate.*

1.4. Objective and structure of the thesis

In this work we studied the vapor phase coating and infiltration (VPI/SCIP) of conductive polymers with inorganics to create new hybrid materials with a higher TE performance. For this aim, several objectives have been established:

- Characterization and *in-situ* QCM studies of Bi_2S_3 ALD using H_2S and $BiCl_3$.
- VPI of conductive polymers (PANI and PEDOT:PSS) with Bi_2S_3 and *in-situ* QCM studies of infiltration.
- Characterization of infiltrated polymers:
    - FTIR analysis;
    - TEM/SEM imaging;
    - EDX mapping.
- Studying of the properties of the obtained hybrid coatings: Conductivity measurements.

These objectives have been developed in four different chapters, as described below.

Firstly, an introduction provided a brief background, an overview of the ALD and VPI coating technologies with a description of the techniques, and the objective and structure of the thesis.

The second chapter – the experimental part - is focused on the description of experimental techniques, characterization tools and equipment, involved in this research. Also, the preparation of the conductive polymer films is described here.

In the third chapter, *in-situ* QCM studies of Al_2O_3 VPI of two conductive polymers, i.e. poly(3,4-ethylenedioxythiophene):poly(styrenesulfonate) (PEDOT:PSS) and polyaniline (PANI), using TMA and H_2O, are studied.

The fourth chapter describes the PEDOT:PSS VPI process by Bi_2S_3 using $BiCl_3$ and H_2O. The change of composition and structure of the infiltrated PEDOT:PSS after various cycles and its stability under the exposure to high temperatures and vacuum environment was investigated. Based on the *in-situ* QCM monitoring results and ex-situ film studies, an infiltration scheme is proposed.

Finally, a summary of the research and future perspectives are given in the conclusions.

2. EXPERIMENTAL

2.1. Custom built ALD/VPI machine

ALD and VPI have been performed in a home built hot-wall viscous flow reactor (see figure 5). Ultrahigh purity nitrogen (99.999%) was used as carrier gas that was injected through a mass flow controller. The nitrogen pressure in the reactor was maintained at 0.9 Torr (~120 Pa) with a nitrogen flow of 200 sccm (standard cubic centimeter per minute).

The reactor chamber was heated with an external heater (oven) providing temperature uniformity that ensures uniform coating thickness. The substrates were placed on a substrate holder inside the rector chamber. The reactor manifold was composed of four dosing lines. The time for a complete cycle depended on the time sequence or recipe which is defined by a/b/c/d/e/f where a is a first precursor pulse time, b is the exposure time for this first precursor, c is the purge time with nitrogen, d is the second precursor dose time, e is the exposure time of a second precursor and f is the purge time with nitrogen.

The precursors were kept in stainless steel cylinders and were in vapor or liquid state. The cylinders were then attached to the ALD dosing valves which supplied the precursor vapors to the reactor chamber. Precursors with a low vapor pressure at room temperature were heated prior to being pulsed into the reactor to ensure a sufficiently high vapor pressure. The temperature of each cylinder was regulated using heating elements and was monitored in real time using a thermocouple.

The manifold was heated to a higher temperature than the cylinders, but lower than the reactor. It is critical to have a temperature gradient from the precursor cylinders to the reaction zone to prevent condensation within the manifold and obstruction of the lines during the pulses. The whole system was connected to a vacuum pump.

The setup is equipped for an *in-situ* monitoring of growth and infiltration processes using a quartz crystal microbalance (not shown in the setup scheme). The mass measurements during pulses of reagents were recorded using a QCM sensor connected to the controller and to a personal computer.

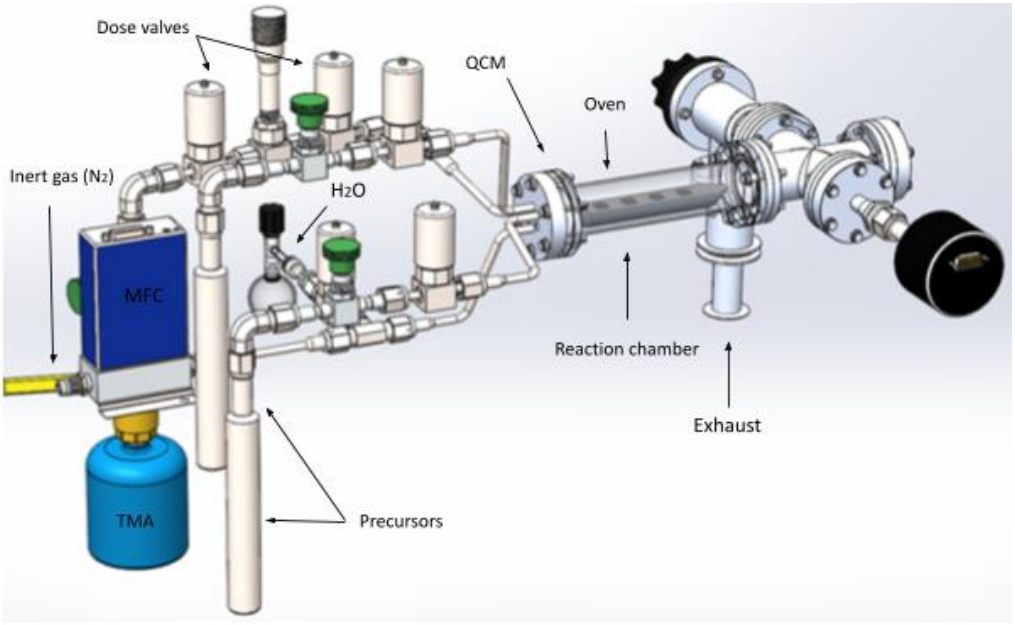

Figure 5. *Schematic diagram of laboratory hot-wall reactor.*

2.2. In-situ Quartz crystal microbalance (QCM)

2.2.1. QCM basis

The QCM technique allows to record changes in the frequency of mechanical vibrations of a piezo crystal, caused by small mass changes observed during the formation of monomolecular and atomic layers during ALD and VPI with a mass resolution of 0.3 ng/cm^2. QCM was used to study the surface reactions and determine the linearity of the film growth during the ALD processes. For VPI processes the QCM was used to quantify the inorganic precursor loading into the polymer bulk and to detect saturation of the sorption. *In-situ* QCM measurements were performed using a polished gold-plated AT-cut quartz crystal (Phillip Tech.), with the resonant frequency 6 MHz. The QCM crystal was installed into the housing, after which it was annealed from 90 to 230 °C to sinter the epoxy resin.

2.2.2. Basis on in-situ QCM testing with ALD Al_2O_3

The temperature profile and thermal effects for the reactor must be analyzed to correctly assess the QCM data before any full-length procedure can take place. QCM proves especially helpful for VPI, as it allows the measurement of the mass gain during each precursor pulse. It can also show the saturation limits of each porous substrate. The mass gain for VPI cannot be calculated from the total thickness of the deposited film using other methods, due to the formation of a hybrid interface on the subsurface of the material and the irregularity of the pores.

The QCM sensor is highly sensible to thermal changes. Al_2O_3 is the most used compound in ALD, being helpful to test the temperature-induced mass changes with H_2O and $Al(CH_3)_3$. There are different, as called, external temperature profiles such as hot, cold, and tuned as shown in figure 6 and in its enlarged view in figure 7. The difference between the precursor gas temperature and the QCM sensor temperature causes apparent mass changes during the gas pulse. In addition, there is a net apparent mass drift after the pulse, which can also be related to the exothermicity of chemical reactions happening on the crystal surface. The thermal effects are also linked to the temperature profile of the reactor, i.e., the temperature gradient along the length of the reactor. Colder temperatures on the reactor section prior to the QCM lead to positive apparent mass changes, while hotter temperatures lead to negative apparent mass changes. [14]

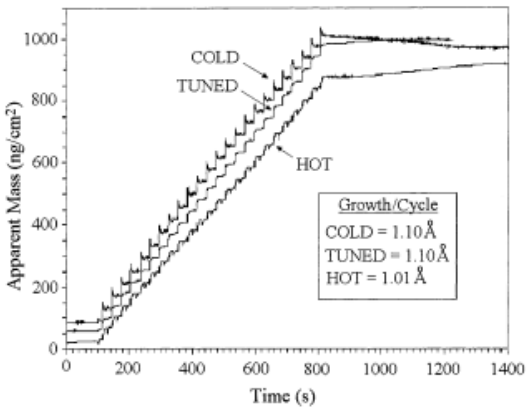

***Figure 6**. Apparent mass (ng/cm²) versus time (s) during Al_2O_3 ALD at 170ºC for hot, cold, and tuned external temperature profiles using H_2O and TMA.* [14]

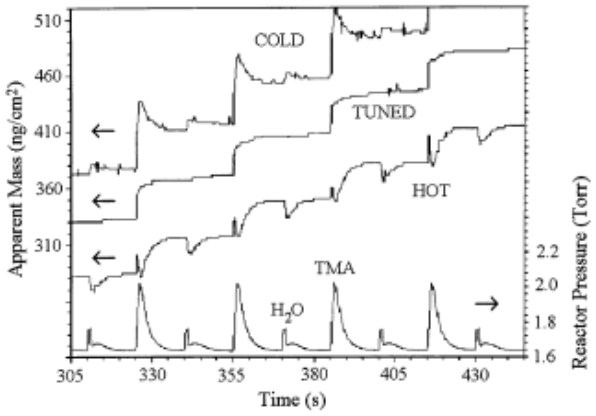

Figure 7. *Enlarged view of Figure 6. The change in reactor pressure is given for the cold profile.* [14]

That shows that the QCM crystal is very sensitive to thermal fluctuations and temperature-induced apparent mass changes can be misinterpreted as resulting from adsorption/desorption processes.

2.3. Fourier Transform infrared spectroscopy (FTIR)

Fourier transform infrared spectroscopy (FTIR) is a non-destructive spectroscopic technique that provides the absorption or emission originating from the bonding characteristics of a material in solid, liquid or gas state. It allows to identify different chemical functional groups of the sample. The main difference between the IR and the FTIR is that the FTIR uses the mathematical Fourier transformation to translate the raw data which are collected through a Michelson interferometer into the actual spectrum. In this technique an IR radiation incises into a beam splitter which separates the beam into two. One of the beams passes to a fixed mirror and the other beam to a mirror which moves with at a certain velocity. These two beams are reflected and recombined before passing the sample, and the transmitted portion of the interferogram is sent to the detector. When the molecule absorbs a photon with an energy shown in equation 2.

$$E = h \cdot v \qquad (2)$$

Where h is the Planck constant and v is the frequency of radiation, specific molecular vibrations modes are generated depending on the nature of the bond. This equation is known as Planck's law.

The infrared spectrum appears as a plot of the absorbance (or % transmittance) versus the wavenumber (cm^{-1}). The frequency ranges are measured as wavenumbers typically from 600 to 4000 cm^{-1}. [15]

The attenuated total reflectance (ATR) is one of the most used techniques to measure FTIR spectra of solid an/or non-transparent samples. Figure 8 shows a schematic of ATF-FTIR where the sample is placed atop an ATR crystal practically without previous treatment.

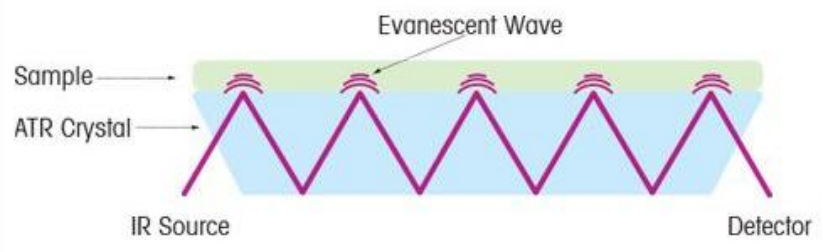

Figure 8. *A schematic diagram of the Attenuated Total Reflectance (ATR).* [16]

An IR light incises with a certain angle known as critical angle on an ATR crystal which is in contact with the sample. The crystal allows total internal reflections of the IR beam, once or multiple times, depending on the crystal. This total internal reflection is produced when the infrared beam on the enter has a higher reflection rate than on the exit when the angle of incidence exceeds the critical angle. This reflection generates an evanescent wave on the surface of the crystal that spreads into the sample as deep as few micrometers (0,5–3 μm). [15] When the sample absorbs energy, the evanescent wave decays exponentially. The reflected light carries the absorption information of the sample and is collected by an IR detector.

In this work, FTIR measurements were performed with a Fourier Transform Infrared (FTIR) spectrometer (FT-IR spectrometer Frontier, PerkinElmer) equipped with a Universal ATR Sampling Accessory.

2.4. Scanning Electron Microscopy (SEM) and Transmission Electron Microscopy (TEM)

Electron microscopy is a useful imaging technique for the analysis of nanomaterials as it offers a magnification of the specimen to a great extent. A Scanning Electron Microscope (SEM) works by emission and release of electrons to obtain an image of the surface of the sample in a small scale to characterize it. Figure 9 (a) shows the key components of a SEM microscope: the electron source and accelerating anode that compose the electron gun, magnetic lenses that are later used to focus the electrons to a specific spot, vacuum chamber which houses the specimen stage and finally, the section of detectors where the electrons get released after getting excited when they reach the surface of the sample. The surface can be “structured” with

the information given by those reflected electrons creating a digital image. For the electrons to be released, the material must be conductive enough because otherwise it can get burned by the high energy that arrives by the electron beam. To avoid this, a conductive coating is applied to the materials surface as a thin layer. [17]

The Transmission Electron Microscopy (TEM) is used for particles, fibers, and thin films to obtain the specimens internal microstructure and for imaging of atoms. Figure 9 (b) shows the layout of a TEM that consists of the electron source and accelerating anode which enable the electron beam to penetrate the material with much higher electron energies than in SEM, electron lenses to focalize the electrons before and after the sample and a parallel recording device such as charged coupled device (CCD). [17]

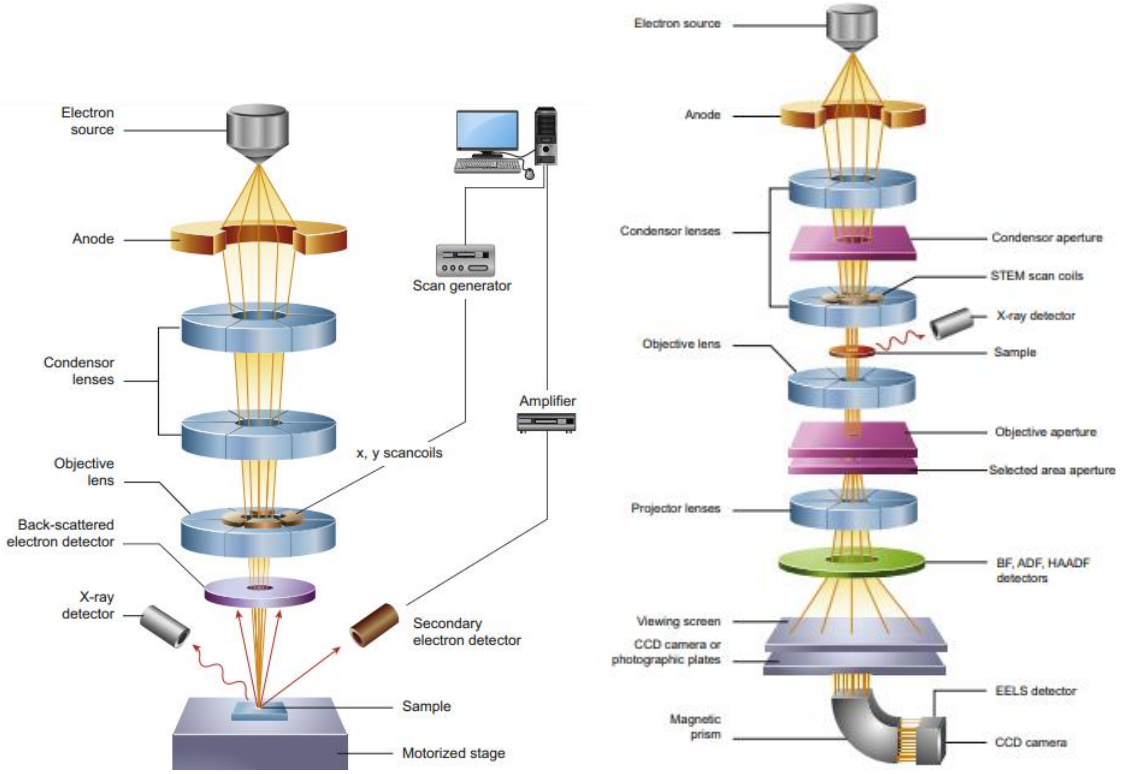

***Figure 9**. (a) Schematic of the Scanning Electron Microscope on the left, (b) Schematic of the Transmission Electron Microscope on the right.* [17]

Scanning transmission electron microscopy (STEM) is a hybrid between SEM and TEM. It combines the principles from both and can be performed on either type of instrument. [17] In this case, the sample is scanned by deflection coils and the electron beam is focused to an Angstrom-sized probe. A bright-field or dark-field STEM image can be formed depending on the transmitted electrons that are used to form the image. [18]

For the preparation of the sample, a little amount of zirconia nanoparticles was suspended in ethanol and the solution was well dispersed.

The precursor penetration depths were surveyed by cross-sectional analysis applying FIB-SEM (Focused Ion Beam Scanning Electron Microscopes). For the SEM tests in this thesis the Helios NanoLab TM Dual Beam TM was employed. It includes a high-resolution Focused Ion Beam (FIB) column, advanced gas chemistry, and the sub-nanometer precision mechanics. TEM imaging analysis was carried out in Titan TM G2 60-300 with an EDX SDD detector.

2.5. Energy dispersive X-ray spectroscopy (EDX)

Energy dispersive X-ray spectroscopy (EDX), also referred to as energy dispersive X-ray analysis (EDXA) or energy dispersive X-ray microanalysis (EDXMA), is an analytical technique applied along with SEM or TEM used to analyze the elemental composition of the materials. It is composed by three main parts which include an X-ray detector, a pulse processor, and a computer system. The impact of an electron beam on the sample's surface causes the emission of X-rays from the material which are then intercepted by the X-ray detector. The emitted X-rays from the sample are generated in function of the characteristics and nature of the elements of the substrate. Once the X-rays are detected by the detector, a small current is generated by the X-ray and later transformed into a voltage pulse. This voltage is measured by the pulse processor with respect to X-ray energy due to its dependence on it. If the X-ray energy of the sample is small, the weak signals can be enhanced by increasing the angle of the detector, increasing imaging times or using higher beam currents. [19]
For the EDX analysis in this thesis a Titan TM G2 60-300 with imaging Cs-corrector was used, which included different features as X-FEG, monochromator, high-resolution Quantum GIF, EDX detector, electron bi-prism and Lorenz lens.

2.6. Chemical structure and preparation of poly(3,4-ethylenedioxythiophene): poly(styrenesulfonate) (PEDOT:PSS), polyaniline (PANI) films

Since 1990, great attention has been paid to the polymers known as "electronic polymers". [20] Poly(3,4-ethylenedioxythiophene) (PEDOT) is a low-cost conductive polymer (CP). It has high thermal stability, optical transparency, high mechanical flexibility, and low density (1,011 g/cm^3). [21] Even though most of the conductive polymers are insoluble, thanks to the limited solvent solubility PEDOT can be emulsified with poly(styrenesulfonate) (PSS) in water getting PEDOT:PSS (figure 10). It is formed by doping PEDOT with positive anions and PSS with negative anions. Due to coulombic attraction, the short PEDOT chains with molecular weight of 1000-

2500 g/mol align with the longer PSS molecular weight of 400 000 g/mol. As a result, PEDOT:PSS becomes a polyelectrolyte with PEDOT being hydrophobic and PSS hydrophilic. It can be dispersed in water and some polar organic solvents. The inorganics used to make PEDOT:PSS-inorganic hybrids are classified in carbon-based and metal-based chemicals like Bi_2Te_3 or Au noble metal nanoparticles. It is widely used in energy-based applications as organic printable electronics and textile electronics.[20], [5], [21]

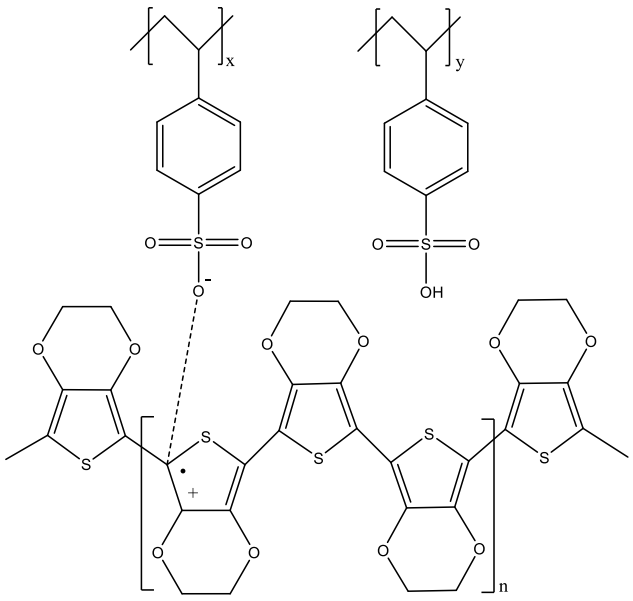

Figure 10. *Schematic of the structure of PEDOT:PSS.*

The next polymer of interest is polyaniline (PANI). Chemically, PANI can change between three idealized oxidation states: leucoemeraldine, emeraldine (emeraldine salt or emeraldine base), and pernigraniline. Polyaniline emeraldine base (PANI-EB) (figure 11) is an intrinsically conductive polymer (ICP) with good stability, formed by oxidative polymerization of aniline. It is one of the most studied conductive polymers. There are already several PANI-inorganic thermoelectric materials reported in literature where PANI is altered by doping it in different ways. The doping can be done with transition metal salts [22], alkali metal salts [23], organic acids [24], inorganic protonic acids [25] or Lewis acids like $SnCl_4$ [26]. The density of PANI at 20 ºC has a value of 1,245 g/cm^3. The glass transition temperature is between 100 and 190 ºC, and the melting temperature is 385ºC. [27] It has several reported applications in different fields such as gas separation, sensor applications and energy storage devices. [20] ,[5] , [28]

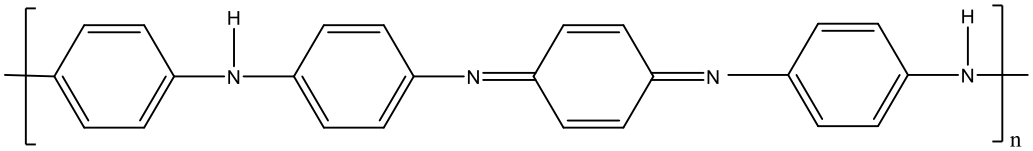

Figure 11. *Schematic structure of PANI-EB polymer.*

The preparation of poly(3,4-ethylenedioxythiophene): poly(styrenesulfonate) and polyaniline films were carried out by drop-casting it in water and in N,N-dimethylformamide (DMF), respectively. Both polymers were supplied by Sigma-Aldrich.

3. QCM STUDIES OF Al_2O_3 VPI OF PEDOT: PSS AND PANI

In this section, VPI of PEDOT: PSS and PANI polymers with Al_2O_3 is characterized and studied *in-situ* by QCM as a test process. Firstly, ALD of Al_2O_3 with TMA and H_2O as precursors is performed with different reactor temperatures, pulse and purge times. A comparative graph is done to analyze the obtained average mass gain per cycle (MGPC) at different deposition temperatures and another one to compare the growth per cycle (GPC) versus exposure time when the reactor temperature is the same. Further, infiltration with TMA and H_2O as single precursors and infiltration with Al_2O_3 is performed in the two different polymers to observe the evolution of the mass gain versus time in each case. Moreover, a comparison between PEDOT: PSS and PANI polymer mass gain is also analyzed.

3.1. Experimental in-situ QCM testing with ALD Al_2O_3

Figure 12 (a) shows *in-situ* QCM MGPC vs. time during 70 cycles at 140 ºC with a timing sequence of 0.1/20/0.1/20 (in seconds), where 0.1s is the precursor dose time and 20s is the purge time. The mass gain obtained during the first 13 cycles of nucleation was significantly higher, which points towards a surface-enhanced growth when the number of reactive sites on the surface of the ALD-material is lower than the ones on the substrate. After these first cycles the system reached linear growth, steady-state regime with a MGPC of 34 ng/cm^2. Figures 12 (b) and (c) show QCM MGPC vs. time during 45 ALD cycles with the timing sequence of 0.5/25/0.5/25 (s) and 35 ALD cycles with the timing sequence of 1/25/1/25 (s) at 140 ºC, respectively. MGPC of 35 ng/cm^2 and 42 ng/cm^2 was obtained at a 0.5/25/0.5/25 and 1/25/1/25 timing sequence respectively. Figure 12 (d) shows the QCM MGPC vs. time during 50 ALD cycles with the timing sequence of 1/25/1/25 (s) at 200 ºC. In all cases a linear and reproducible growth was obtained.

The positive mass spikes in Figure 12 (a), (b), (c) and (d) indicate that the reactor has a cold profile (i.e., the reactor walls are colder than the QCM crystal). The reactor cools down during the dosing of precursor gases and reheats after gas dosing. These apparent mass spikes should be treated as errors in the QCM crystal signal, and the MGPC is measured as the mass increase from a stable baseline to another within each cycle.

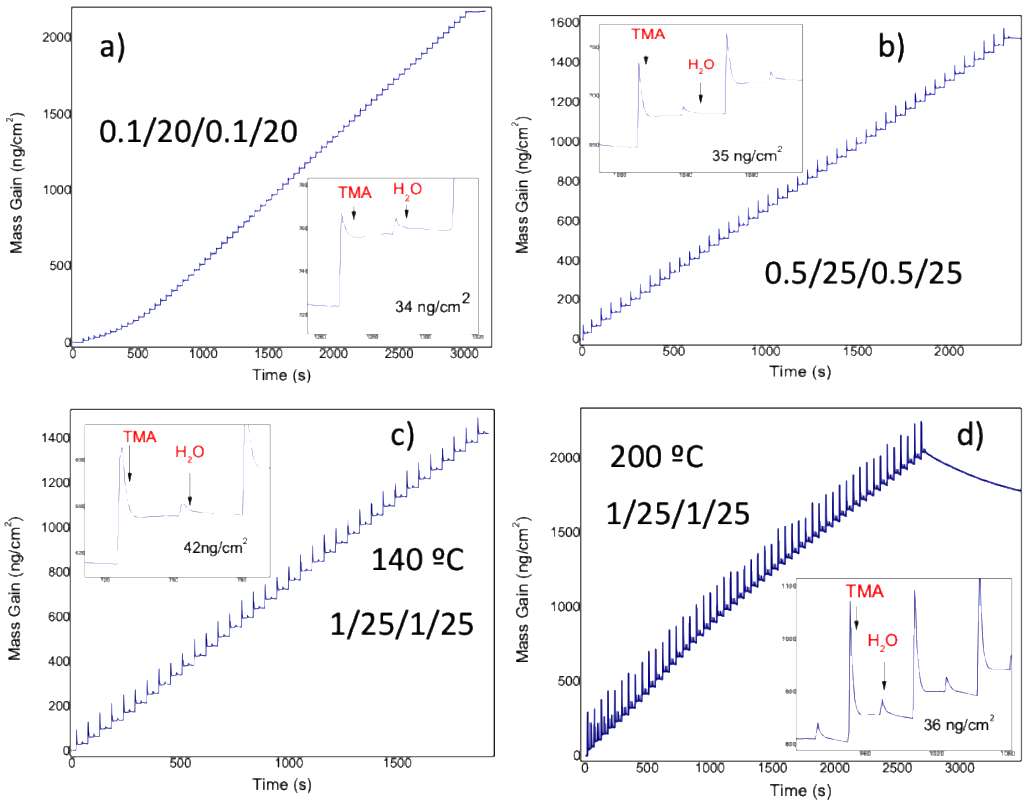

Figure* 12.** *In-situ QCM MGPC (ng/cm^2) vs. time (s) during* **(a)** *70 ALD cycles with the timing sequence of 0.1/20/0.1/20 (s) at 140 ºC,* **(b)** *45 ALD cycles with the timing sequence of 0.5/25/0.5/25 (s) at 140 ºC,* ***(c) 35 ALD cycles with the timing sequence of 1/25/1/25 (s) at 140 ºC, ***(d)*** *50 ALD cycles with the timing sequence of 1/25/1/25 (s) at 200 ºC.*

Figure 16 shows the GPC (ng/cm^2-cycle) vs. deposition temperature (ºC) for the data obtained at 140 and 200 ºC, respectively. The GPC for each case was calculated as the average MGPC in the linear growth regime and showed a value of 42 and 34 ng/cm^2, respectively. It can be observed that, as the deposition temperature increases, the average GPC decreases are being caused by thermodynamics. It shows that there is no "temperature window" where the GPC is constant.

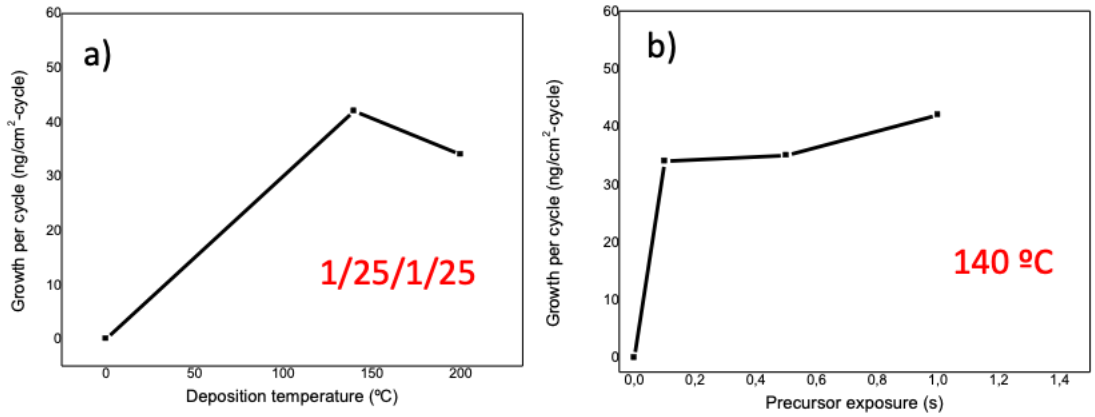

Figure 13. *GPC (ng/cm²-cycle) vs. deposition temperature (ºC) in a steady-state regime* ***(a)****. In-situ QCM GPC (ng/cm²-cycle) vs. precursor exposure (s) at 140 ºC in a steady-state regime* ***(b)****.*

MGPC (ng/cm^2-cycle) versus precursor exposure time (s) is plotted in figure 13 (b) where the experiments were done at the same reactor temperature of 140 ºC to study the self-limiting behavior of the surface reactions. The GPC values have been extracted from Figures 12 (a), (b) and (c) as the average MGPC in a steady-state regime. GPC of 34, 35 and 42 ng/cm^2 was obtained for 0.1, 0.5 and 1 sec precursors dose respectively. It can be seen that as the precursor exposure time increases from 0.5 to 1 s, the MGPC continues to increase. This doesn´t correspond with the idea of self-limiting behavior of the surface reactions. This could also indicate that the volume of the reactor chamber was big.

3.2. In-situ QCM studies of PEDOT: PSS VPI using TMA and H_2O

In-situ QCM studies are performed to see how mass gain changes with the time when using TMA or H_2O as single precursors for the PEDOT: PSS polymer. 36 cycles at 110 ºC were performed with the time sequence of 0.4/40/0.4/40 (s) where 0.4 s correspond to the TMA and H_2O pulses and 40 s to the N_2 purge time after each precursor pulse. Figure 14 shows the MGPC vs. time (s) during 36 cycles of VPI of PEDOT:PSS using TMA precursor (a) and H2O precursor (b) at 110 ºC. During the PEDOT: PSS infiltration, a first dose of TMA led to a large mass gain value of 500 ng/cm^2, followed by a slower infiltration rate. 36 doses of TMA resulted in a nearly saturated mass gain of 1093 ng/cm^2. In each TMA dose, the mass loss occurs after the mass uptake, which can be explained with the diffusion-desorption process being partly reversible. In figure 14 (b), the PEDOT: PSS VPI using H_2O pulses only is resulting in a negative mass gain of -1205 ng/cm^2 after 36 cycles and the etching process has a linear-like behavior. PEDOT: PSS etching is caused by the H_2O exposure can be explained with a polymer dissolution process, as the polymer is

soluble in water. H_2O soaks the polymer and during purge step it is removing mass from the PEDOT: PSS substrate.

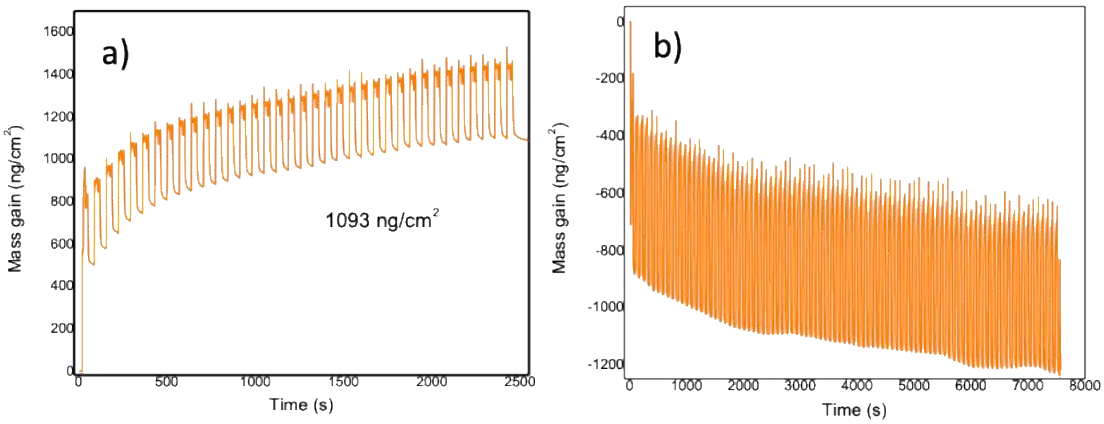

Figure 14. *In-situ QCM MGPC (ng/cm²) vs. time (s) during 36 cycles of PEDOT:PSS VPI using TMA precursor at 110 ºC (a). In-situ QCM MGPC* (ng/cm²) vs. time (s) 36 cycles PEDOT:PSS VPI using H_2O precursor at 110 ºC **(b)**.

After single-precursor infiltration, Al_2O_3 infiltration was performed. The *In-situ* QCM mass change vs. time during 10 VPI cycles using H_2O and TMA pulses at 110 ºC with PEDOT: PSS as a substrate is shown in figure 15. Th TMA pulse leads to a mass gain, while the H_2O dose leads again to a slight mass decrease. The resulting Al_2O_3 mass gain upon VPI of PEDOT: PSS is 175 ng/cm^2. This is considerably higher than the growth rate of an Al_2O_3 ALD coating process.

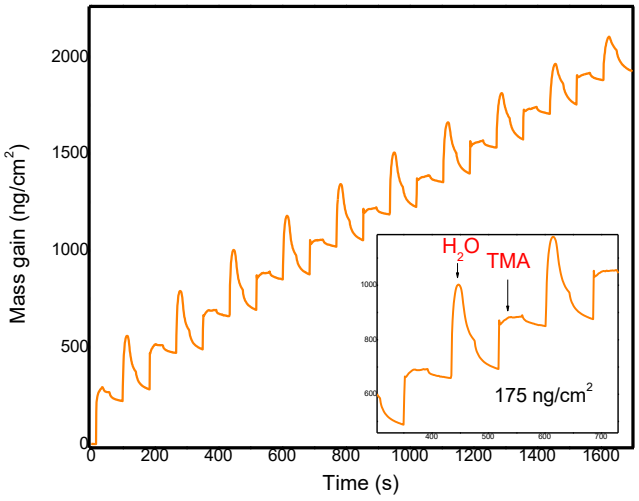

Figure 15. *In-situ QCM mass gain (ng/cm²) vs. time (s) during 10 Al_2O_3 VPI cycles with TMA-H_2O pulses at 110 ºC.*

3.3. In-situ QCM studies of PANI VPI using TMA and H_2O

As in PEDOT: PSS, *in-situ* QCM studies were performed for PANI VPI to see how mass gain develops with time using TMA and H_2O as single precursors. Both processes were done at the same temperature of 110 ºC with a time sequence of 0.4/20/30 seconds during 70 cycles with 0.4 s being the pulse time, 20 s the exposure time and 30 s the purge time. Figure 16 (a) shows the MGPC vs. time for the VPI of PANI with TMA. A mass gain saturates at 267 ng/cm^2, which is 4 times lower than in the case of PEDOT: PSS. Figure 16 (b) shows *in-situ* QCM data of PANI VPI using H_2O as precursor. The resulting mass gain saturates at 57 ng/cm^2 after 70 cycles of the process with a slight mass loss after the process, determined as unreacted precursor desorption from the polymer bulk. The fact that PANI VPI with H_2O leads to a positive mass gain confirms that the PEDOT:PSS etching with H_2O is governed by polymer dissolution-desorption process.

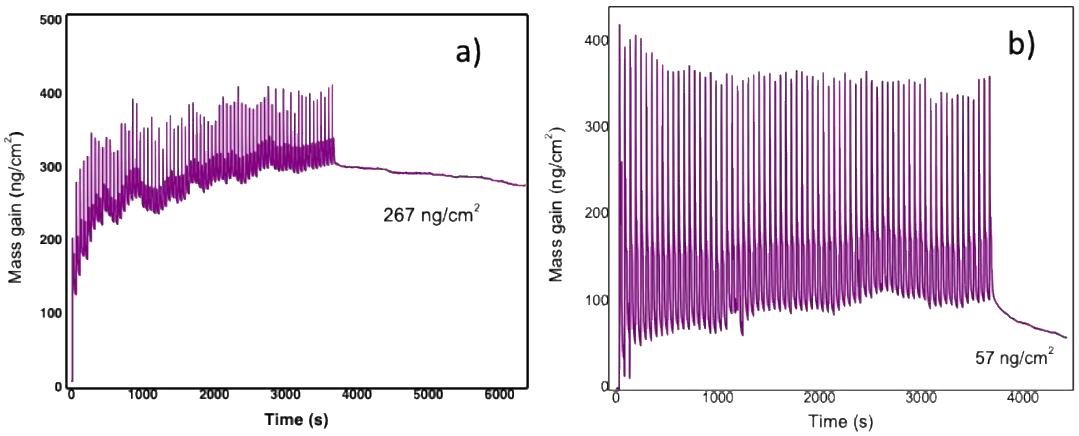

Figure 16. *In-situ QCM mass gain (ng/cm^2) vs. time (s) during 70 cycles of VPI of TMA into PANI at 110 ºC* ***(a)****. In-situ QCM mass gain (ng/cm^2) vs. time (s) 70 cycles of VPI of H_2O into PANI 110 ºC* ***(b)****.*

The *In-situ* measured QCM mass changes vs. time with PANI as substrate during 15 cycles of H_2O and TMA pulses at 110 ºC are shown in figure 17. The time sequence consists of TMA pulse (0.4 s), exposure time (60 s), purge time with nitrogen (70 s), H_2O pulse (0.4 s), exposure time (60 s) and purge time with N_2 (70 s). Both precursor doses result in a mass increase with a total MGPC of 141 ng/cm^2.

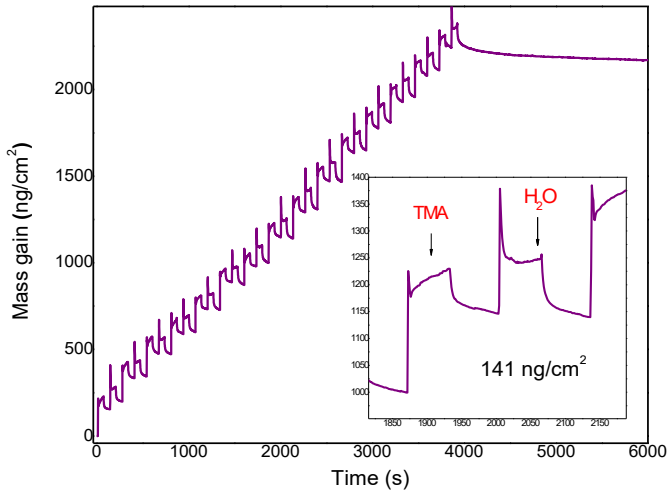

***Figure 17**. In-situ QCM mass gain (ng/cm²) vs. time (s) of 15 VPI cycles of PANI with TMA-H_2O 0.4/60/70/0.4/60/70 at 110 ºC.*

Finally, a comparison between the mass gain versus time for both polymers (PEDOT: PSS and PANI) is shown in figure 18. PEDOT: PSS showed a higher infiltration rate than PANI. This can be due to the higher number of reactive sites (to TMA) in PEDOT:PSS (figure 10) than in PANI (figure 11). Also, the density of PEDOT:PSS is lower than the density of PANI (2.6. section), which can cause a better diffusion and infiltration.

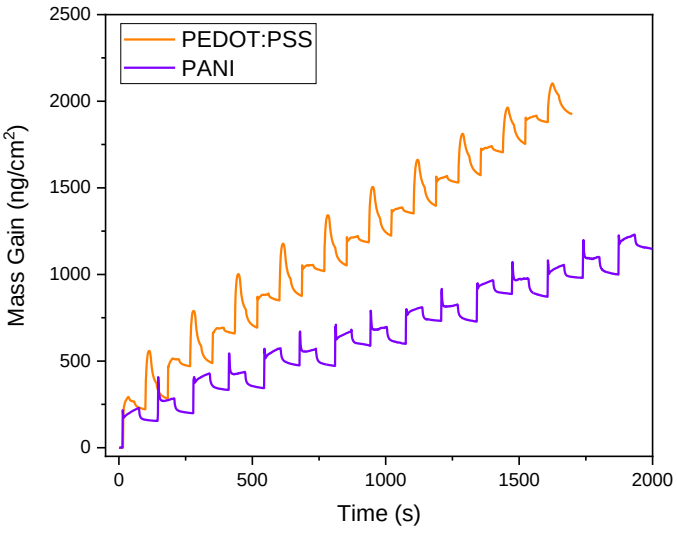

***Figure 18**. In-situ QCM mass gain (ng/cm²) vs. time (s) for PEDOT: PSS (orange) vs PANI (purple) upon Al_2O_3 VPI at 110 ºC.*

4. VPI PROCESS OF PEDOT: PSS and PANI BY Bi_2S_3 USING $BiCl_3$ AND H_2S

This chapter describes an ALD and a VPI process to dope PEDOT: PSS and PANI by Bi_2S_3 using $BiCl_3$ and H_2S as precursors. The chemical changes resulting from the infiltration of PEDOT: PSS and PANI by Bi_2S_3 are characterized with *in-situ* QCM measurements, FTIR, SEM and TEM.

4.1. Experimental part

ALD and VPI depositions were performed in a custom made hot-wall reactor shown in figure 5. The experiments were carried out at a constant reactor temperature of 150 or 155 ºC with a baseline reactor chamber pressure of 1 torr and a constant N_2 flow of 150 -200 sccm. Each cycle was composed of a pulse, exposure, and purge sequence for each precursor. The $BiCl_3$ and H_2S precursors were purchased from Sigma-Aldrich. $BiCl_3$ was heated to 140 ºC and had a pressure of 1 torr while H_2S was not heated and was set a to a pressure of 2 torr. The H_2S cylinder (kept at room temperature) was filled with liquid H_2S under high pressure using liquid N_2 to condense it into the steel container. The preparation of the substrates for infiltration was described in section 2.7.

Silicon (Single-side polished P-type silicon (100) wafers) and glass (Corning Glass, 1mm thickness) substrates were sonicated for 30min in an acetone cleaning solution, rinsed with acetone, water and ethanol and dried with a N_2 flow gun. Zirconium oxide nanoparticle (NPs) pellets were prepared for the ATR-FTIR analysis. For the TEM samples, a zirconium oxide NP suspension in ethanol was drop-casted onto Protochip Lacey Carbon gold and copper grids.

For the *in-situ* monitoring of the Bi_2S_3 growth and infiltration processes, piezoelectric crystals with polished gold-plated electrodes were used as substrates. The ALD processes were performed at different processing conditions (Table 1) using piezoelectric crystals (Coltanec 6MHz, 14mm, Polished High Freq. Gold Quartz Crystals) inserted into the QCM sensor to obtain the GPC at the given condition.

ATR-FTIR spectra of the samples were carried out with a PerkinElmer Frontier spectrometer. Pressed nanopowder of Zirconium (IV) oxide (Sigma-Aldrich, <100 nm) was used as a substrate to increase the coated surface area and thus the signal-to-noise ratio. The spectra were recorded between 600 and 4000 cm^{-1}.

The morphology examination of the samples was done with a scanning electron microscope in a Dual-beam FIB/SEM – FEI Nanolab/ FEI Helios 450S. For SEM cross-section studies, to protect the sample surface before ion beam deposition, a Pt layer was used on top before FIB cutting.

TEM images were recorded with a TitanTM G2 60-300, equipped with an EDX SDD detector. The voltage was 300 kV.

4.3. ALD of Bi_2S_3 using $BiCl_3$ and H_2S

The proposed scheme for the two-step ALD reaction of H_2S and $BiCl_3$ is shown in figure 25. The process is based on sequential surface reactions between $BiCl_3$ and H_2S. Firstly, the surface with the functional hydroxyl OH groups is exposed to $BiCl_3$. During reaction (A), H_2S is dosed to the Bi-chlorinated surface where the chlorine ligand of the bismuth is replaced to SH group. In step (B), $BiCl_3$ is exposed to the -SH functionalized surface, which leads to an electrophilic attack of the surficial thiol groups by Bi, regenerating the Bi-Cl. HCl is released as by-product in both reactions.

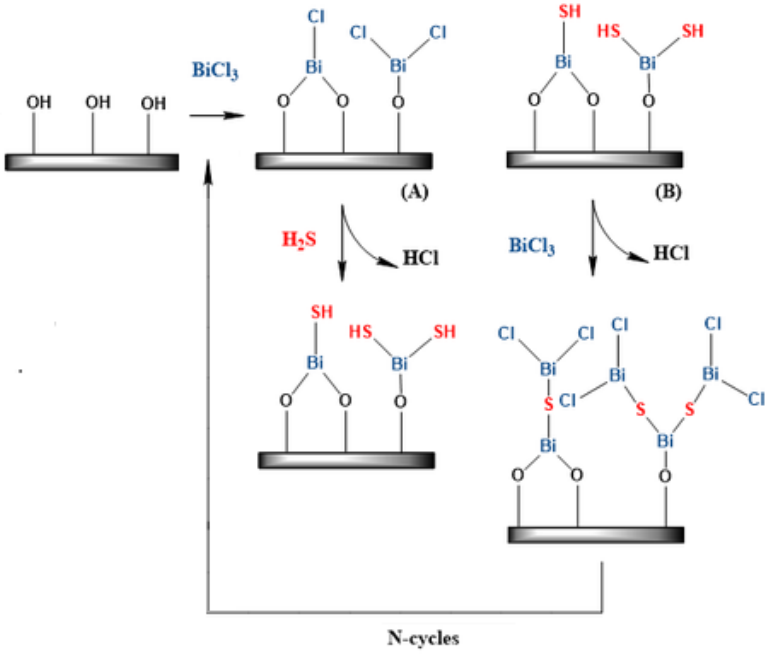

Figure 19. *Schematic of the proposed two-step mechanism of the Bi_2S_3 ALD growth using H_2S and $BiCl_3$.*

The ALD cycle is then repeated to form a new layer on top. The total thickness of the final film is dependent on the number of applied cycles and the GPC.

In-situ QCM measurements were performed for the ALD deposition of Bi_2S_3 using $BiCl_3$ and H_2S as reactants on the QCM crystal precoated with alumina. Figure 20 shows the *in-situ* QCM mass gain vs. time with a sequence of 4/20/0.02/20, with 4 and 0.02 s being the pulse times of $BiCl_3$ and H_2S, respectively, and 20 s the purge time. 40 cycles were performed at 150 ºC and showed around 2 ng/cm^2 MGPC in a steady state growth regime. During the first 12 nucleation cycles the growth rate was higher, indicating a substrate-enhanced growth mode.

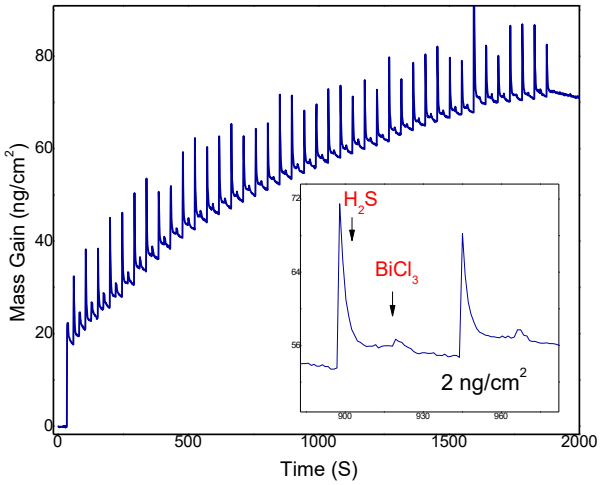

Figure 20. *In-situ QCM mass gain (ng/cm²) vs. time (s) of Bi_2S_3 ALD using $BiCl_3$ and H_2S precursors during 40 cycles with a time sequence of 4/20/0.02/20 (s) at 150 ºC.*

In addition, we performed further *in-situ* QCM measurements using multiple precursor exposures at 155 ºC. In figure 21 (a) several exposure steps were done during 13 cycles in a time sequence of 4/10 (s) during 6 exposures, 15 seconds of waiting and 0.02/10 (s) during 5 exposures. The 4 corresponds to the $BiCl_3$ pulse time, the 0.02 to the H_2S pulse time, each followed by a 10 s purge. A total mass gain per cycle of 4 ng/cm^2 was obtained. Figure 21 (b) shows the mass gain (ng/cm2) vs. time (s) of Bi_2S_3 using $BiCl_3$ and H_2S precursors during 18 cycles in a time sequence with 2 s pulses and 4 exposures to $BiCl_3$ and 0.02 s pulses and 3 exposures to H_2S at 155 ºC. The resulting MGPC was 3 ng/cm^2, showing that longer precursor pulses cannot significantly increase the Bi_2S_3 ALD growth rate.

The achieved low MGPC values can be due to island growth i.e., there is no formation of a continuous layer.

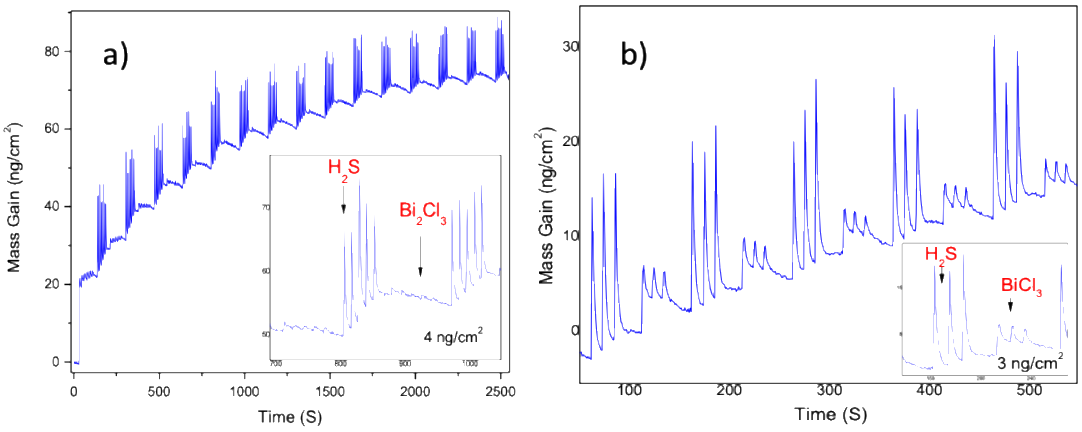

Figure 21. *In-situ QCM mass gain (ng/cm²) v.s time (s) for Bi_2S_3 using $BiCl_3$* and H_2S precursors during 13 cycles in a time sequence where several exposures*:* 4/10 (s) 6 exposures *($BiCl_3$)*, 15 s waiting time and 0.02/10 (s) 5 exposures *(H_2S)* at 155 ºC **(a)**; mass gain (ng/cm²) vs. time (s) of Bi_2S_3 *using* $BiCl_3$ and H_2S precursors during 18 cycles in a time sequence with several exposures 2 s 4 exposures *($BiCl_3$)* and 0.02 s 3 exposures *(H_2S)* at 155 ºC **(b)**.

Figure 22 shows the ATR-FTIR spectrum of the ALD-deposited Bi_2S_3 film from H_2S and $BiCl_3$ precursors within the range of 4000-600 cm^{-1}. Initially, a background spectrum of pure ZrO_2 nanoparticles was recorded and subtracted from the spectra of the sample. The broad band around 3400 cm^{-1} is attributed to the stretching vibration of O-H due to the presence of moisture and the band at 1533 cm^{-1} is due to the bending mode H– O–H. [29] At 2959 cm^{-1} an alkyl C-H stretching vibration band is seen. The peak at 1627 cm^{-1} is due to the carbonyl group. The bands appearing around 1257 and 1083 cm^{-1} are associated with the asymmetric S-H stretching vibration. The strong bands at 847, 747 and 659 cm^{-1} correspond to the banding vibration of the Bi-S bond. Similar absorptions were reported by S.V. Prabhakar Vattikuti et. at [30], earlier.

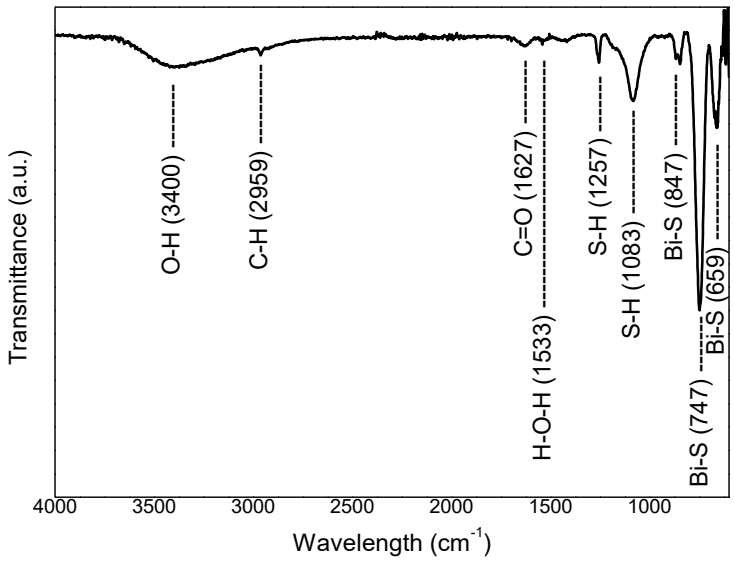

Figure 22. *ATR-FTIR spectra of Bi_2S_3 after ALD reaction with H_2S and $BiCl_3$ as precursors.*

4.4. Results and discussion

4.4.1. Proposed VPI mechanism

Figure 23(a) shows a schematic layout of the PEDOT:PSS/Bi_2S_3 hybrid film growth after VPI of PEDOT:PSS with $BiCl_3$ and H_2S precursors, where PEDOT:PSS is represented with orange and Bi_2S_3 with blue colors. Figure 23 (b) shows the proposed two-step A-B mechanism of the VPI reaction of $BiCl_3$ and H_2S for a PEDOT:PSS-Bi_2S_3 hybrid material growth based on *in-situ* QCM and ex-situ ATR-FTIR, EDX in TEM and SEM analyses. The ATR-FTIR results of the PEDOT:PSS-Bi_2S_3 hybrids showed the presence of newly formed Bi-S bonds after infiltration. The thiophene groups in the polymer have acidic hydrogen that reacts with the $BiCl_3$ to form HCl and new Bi-S bonds during the first self-limiting step of the reaction.

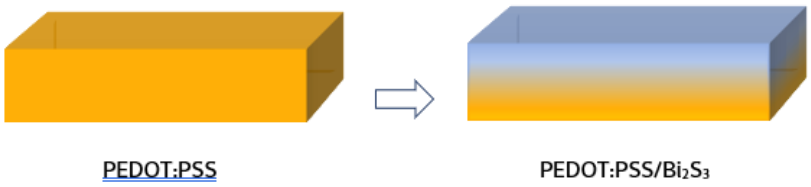

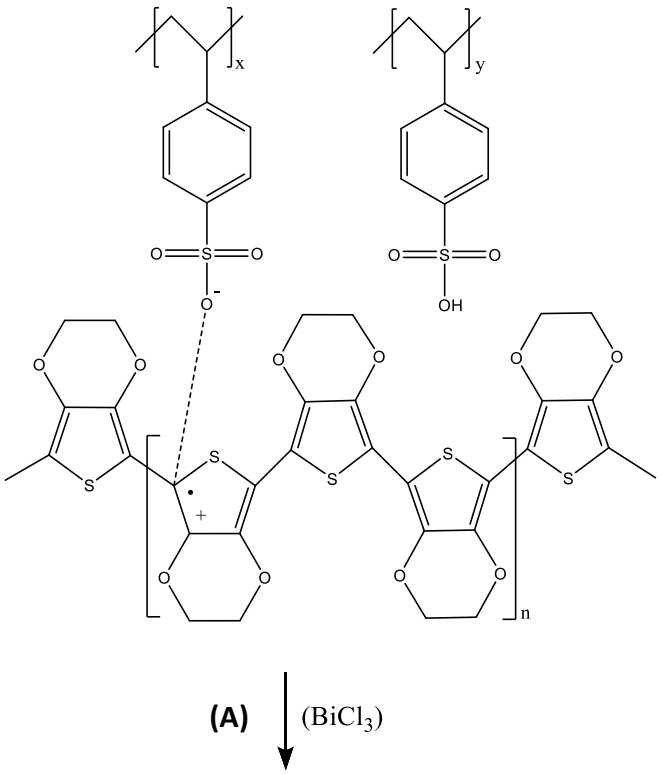

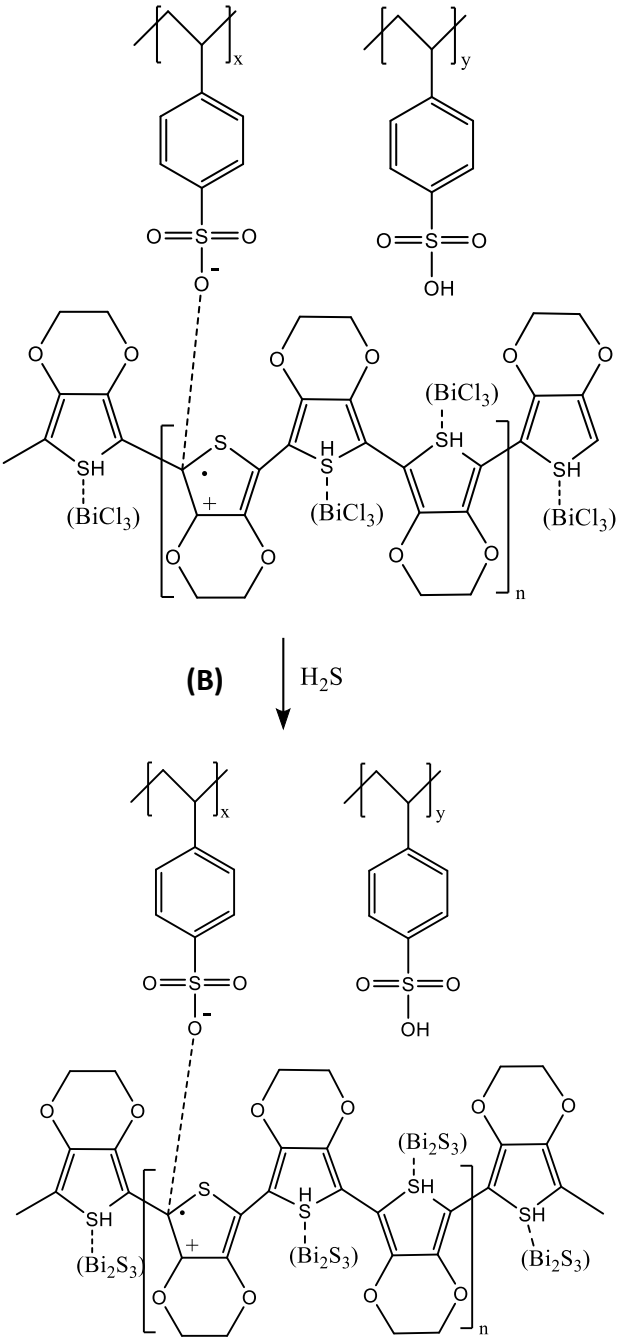

Figure 23**. Scheme of PEDOT:PSS/Bi_2S_3 hybrid material growth after VPI of PEDOT:PSS with $BiCl_3$ and H_2S **(a)**. Proposed mechanism of PEDOT:PSS/Bi_2S_3 hybrid material growth after VPI of PEDOT:PSS with $BiCl_3$ and H_2S. **(b).

Figure 24 (a) shows a schematic representation of PANI infiltrated by $BiCl_3$ and H_2S precursors providing a PANI-Bi_2S_3 hybrid. According to previous publications that were reported on various doping strategies of PANI with Lewis acids [26], the reaction mechanism shown in figure 24 b has been proposed. Initially, PANI emeraldine base contains amine (-NH) and imine (=N) groups, which act as functional groups for binding of $BiCl_3$. Later, H_2S is exposed and reacts with the $BiCl_3$

forming Bi_2S_3. In both half-reactions, when the precursor is exposed, HCl is formed as by-product.

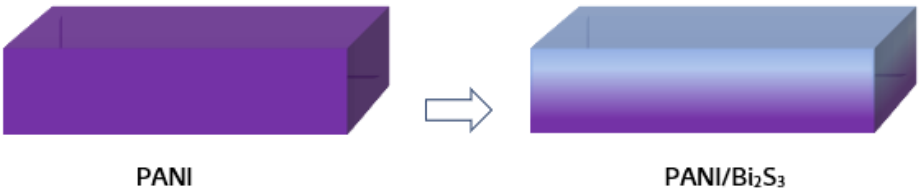

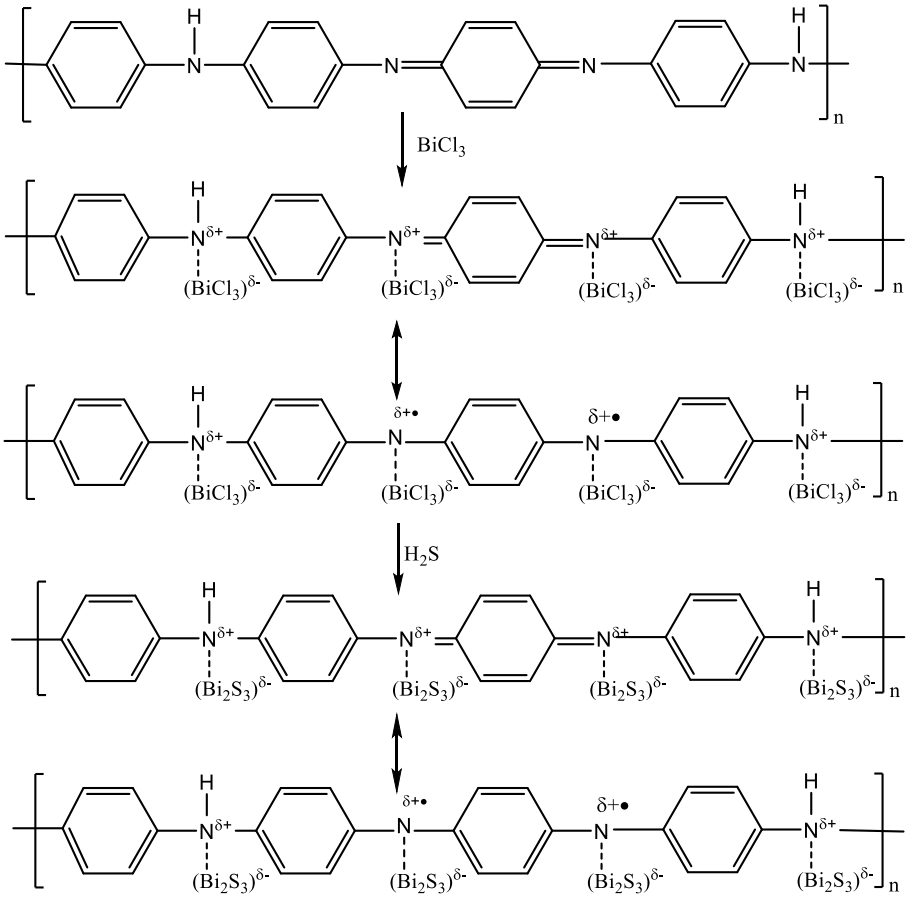

Figure 24**. Scheme of a PANI- Bi_2S_3 hybrid material growth after VPI of PANI with $BiCl_3$ and H_2S **(a)**.* Proposed mechanism of a PANI- Bi_2S_3 hybrid material growth after VPI of PANI with $BiCl_3$ and H_2S ***(b).

4.4.2. ATR-FTIR

ATR-FTIR analysis was performed for annealed polymers (150°C for 2h in vacuum reactor chamber) and for infiltrated polymers at 120°C and 150°C, drop-casted on glass substrates to detect the formation of new chemical bonds.

Figure 25 shows a comparison of the ATR-FTIR spectra of the PEDOT:PSS polymer (orange) and PEDOT:PSS/Bi_2S_3 infiltrated polymer (blue) between 3000 and 650 cm^{-1}. In the spectra obtained from the raw polymer, the broad peak around 1708 cm^{-1} can be attributed to the C=C bond. This peak was not seen in the infiltrated polymer. The observed band at 1267 cm^{-1} is attributed to C-C bond. The peaks at 1126 and 1011 cm^{-1} are assigned to C-O-C and C-O stretching bonds, respectively. The peaks at 699 and 858 cm^{-1} correspond to the C-S bond in PSS and in the PEDOT thiophene ring respectively. [31], [32], [33] The Bi_2S_3-related bands, such as S-H and Bi-S, can also be seen. The S-H bands are at 1209 and 1083 cm^{-1} and the bands corresponding to Bi-S are at 805 and 646 cm^{-1}.

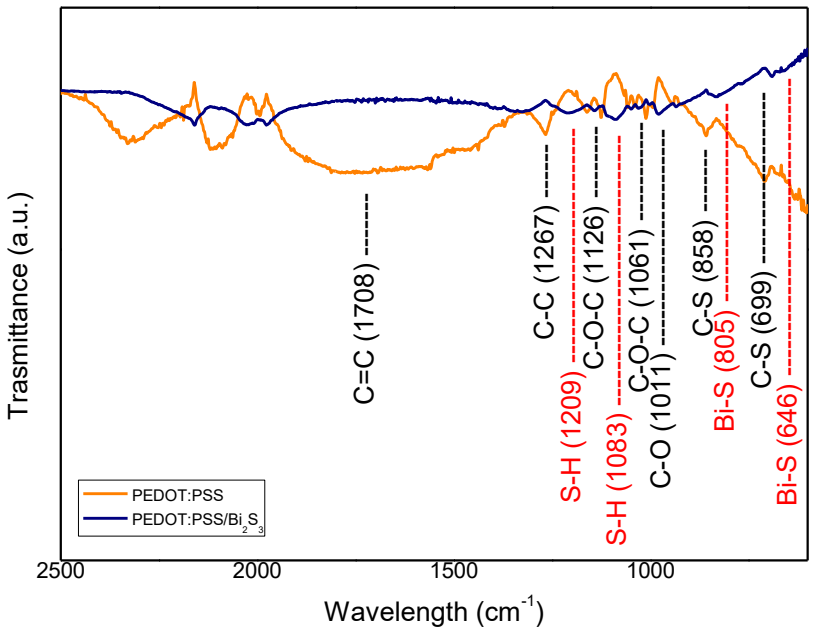

Figure 25. *Comparison of ATR-FTIR spectra of PEDOT:PSS and PEDOT:PSS/Bi_2S_3.*

A comparison of the ATR-FTIR spectra of PANI (purple) and infiltrated PANI with Bi_2S_3 (blue) by VPI is shown in figure 26. The peak around 3043 cm^{-1} represents the N-H stretching peak. The band at 1582 cm^{-1} shows the C=N stretch in a quinoid ring (N=Q=N) while the strong peak at 1497 cm^{-1} represents C=C in a benzenoid ring (N-B-N) where B assigns to the benzenoid type of rings and Q to the quinoid type of rings. To see if the polyaniline is in the emeraldine structure PANI-EB, these two last bands must have comparable intensities because of the oxidation condition of polymerization. In the interval of 1300-1140 cm^{-1}, the C-N bending peaks appear. The band at 1149 cm^{-1} can be attributed to the group vibrations of B-NH-B or B-NH-Q. The band

at 825 cm^{-1} stems from C-H out of plane vibrations of substituted aromatic rings. [34] In addition, the spectra of infiltrated PANI show S-H and Bi-S bands at 1011 and 683 cm^{-1}, respectively.

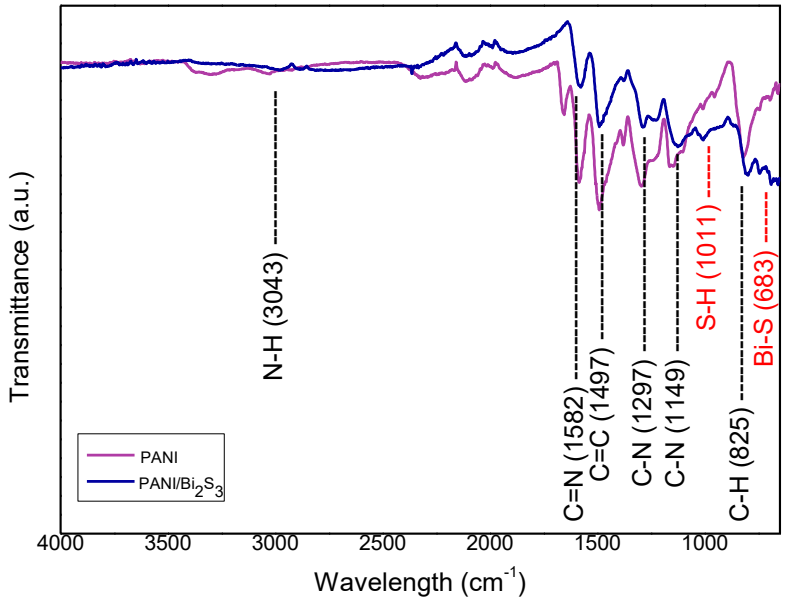

Figure 26. *Comparison of ATR-FTIR spectra of PANI-EB and PANI-EB/Bi_2S_3.*

Unfortunately, the PANI samples become very brittle and detach from the substrates after the processes, making it impossible to analyze the structure and morphology using microscopic techniques. Hence, PANI was not further studied in this thesis.

4.4.3. SEM and TEM

The STEM images showed in figure 27 revealed crystalline orientation of Bi_2S_3.

High-resolution transmission electron microscopy (TEM) and scanning electron microscopy were used to examine the morphology and composition of the ALD film grown at 150 °C on ZrO_2 NP's and on a lacey carbon TEM grid. Zirconia NPs were chosen because of their chemical stability and good contrast in TEM images. Figure 27 shows the TEM images obtained in a scanning regime of the resulting Bi_2S_3 ALD coating. The morphology analysis by TEM revealed that Bi_2S_3 does not form continuous layers, neither on ZrO_2 NPs nor on the pure carbon substrates. The Bi_2S_3 ALD coating rather shows an island-like growth with 10-15 nm sized particles. The growth of ALD films on pure carbon was not expected, as the carbon surface is non-reactive for the ALD film growth. Nevertheless, it may have defects with oxygen-containing functional groups like –OH, -COOH, -C=O and -C-O. Considering that we are using H_2S as co-reactant at 150°C, we may potentially functionalize and activate the carbon surface with sulfur-containing functional

groups like –SH and –C-S. In this case, the thiol group formation would trigger an ALD growth also on the carbon surface. [35]

Another possibility could be that Bi_2S_3 particles, grown on the ZrO_2 surface, could migrate from the hydrophilic ZrO_2 to the rather hydrophobic surface of carbon. To analyze this possibility, we repeated the experiments on pure carbon without zirconia NP. Bi_2S_3 grew also on carbon even in the absence of ZrO_2 NPs. This confirms that the effect is not based on migration, but it supports the theory of carbon surface functionalization with hydrophilic thiol groups.

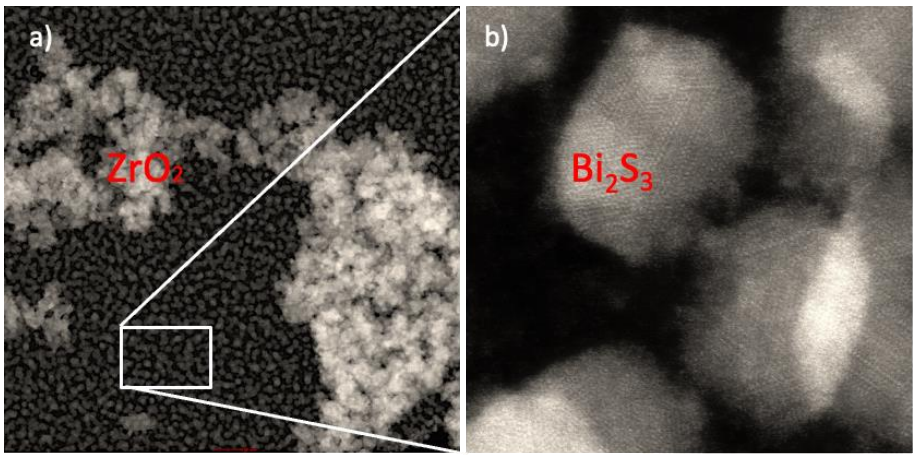

Figure 27. *STEM image of ALD-deposited Bi_2S_3 on ZrO_2 NP on a lacey carbon TEM grid* ***(a)****, Expanded view of the Bi_2S_3 crystals* ***(b)****.*

Figure 28 (a) and (b) also shows STEM and TEM images of Bi_2S_3 deposited on ZrO_2 NPs. [36] ZrO_2 can be seen as a 30-40 nm round shape crystall, while Bi_2S_3 appears as a smaller shape round crystal grown around a ZrO_2 NP.

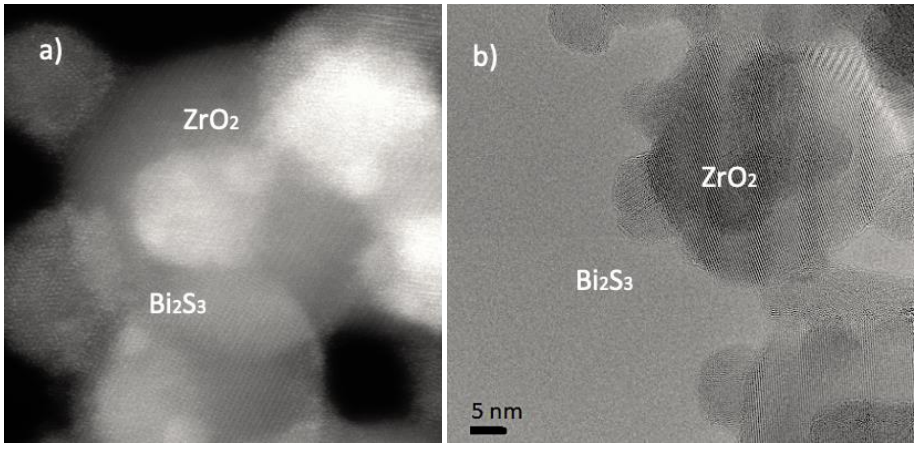

Figure 28*. STEM image of Bi_2S_3 on ZrO_2 grown by ALD* ***(a)****. TEM image of Bi_2S_3 in ZrO_2 grown by ALD* ***(b)****.*

Figure 29 displays SEM images of Bi_2S_3 crystals and Bi_2S_3 coating at the surface of the infiltrated PEDOT:PSS at 150°C after 800 VPI cycles (a,b), Bi_2S_3 crystals and coating at the surface of the

infiltrated PEDOT:PSS and Si substrate boundary (c) and finally Bi_2S_3 crystals and coating at the surface of a Si substrate (d). Clear differences can be observed in the population and shape of the Bi_2S_3 crystals at the surface of the infiltrated PEDOT:PSS and the Si substrate. In the polymer, the infiltrated Bi_2S_3 crystals have a square-shape, around 50 to 200 nm in size. The appearance of the Bi_2S_3 flakes is not as dense as in the case of Si. Crystals tend to grow more on themselves than on the surface in this case. The Bi_2S_3 crystals on the Si surface have a needle-like shape and are around 20 to 160 nm in size.

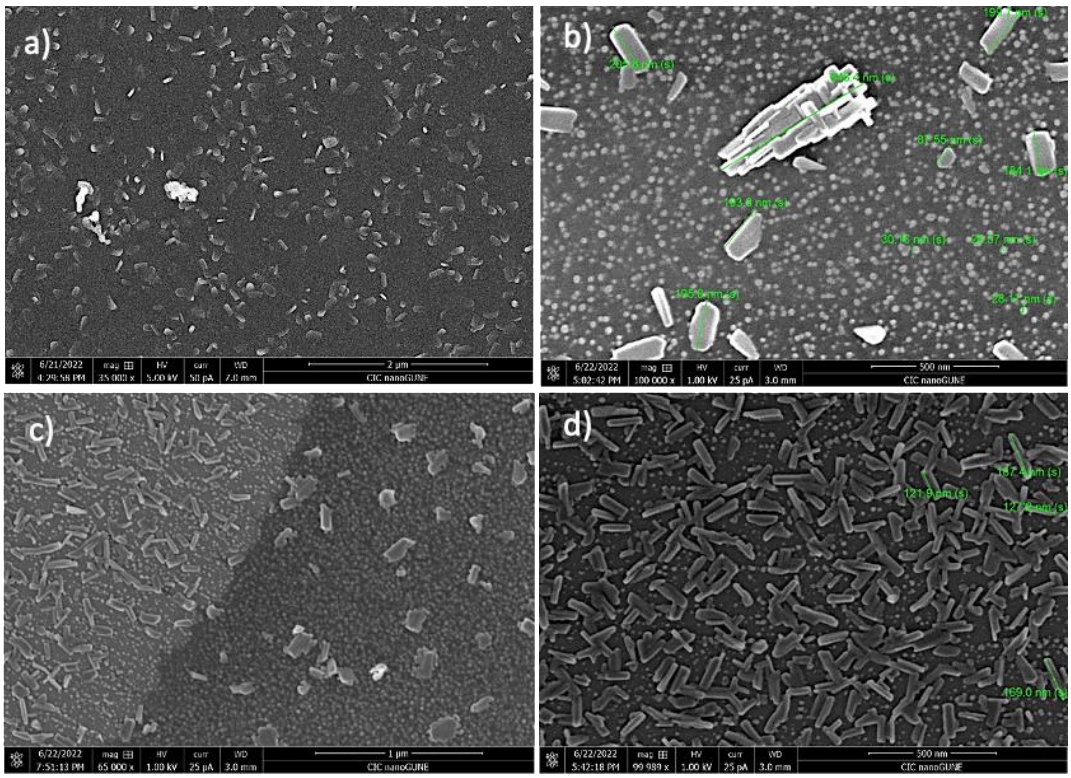

Figure 29. *SEM images of Bi_2S_3 crystals and Bi_2S_3 coating at the surface of the infiltrated PEDOT:PSS at 150°C after 800 VPI cycles* ***(a,b)****. Bi_2S_3 crystals and Bi_2S_3 coating at the surface of the infiltrated PEDOT:PSS and Si substrate boundary* ***(c)****. Bi_2S_3 crystals and Bi_2S_3 coating at the surface Si substrate* ***(d)****.*

The samples were further cut by a FIB to investigate their cross-sections by SEM. Figure 30 shows the SEM images of the cross-section of PEDOT:PSS after 800 cycles of Bi_2S_3 VPI, processed at 150°C. From the expanded view of the cross-section SEM image in Figure 30 (b), the formation of a hybrid layer can be seen as brighter subsurface area, formed only at around 250 nm depth of the polymer after 800 VPI cycles. Note that the total thickness of the polymer was 4.2 µm. The formed hybrid layer confirms successful infiltration of PEDOT:PSS with Bi_2S_3.

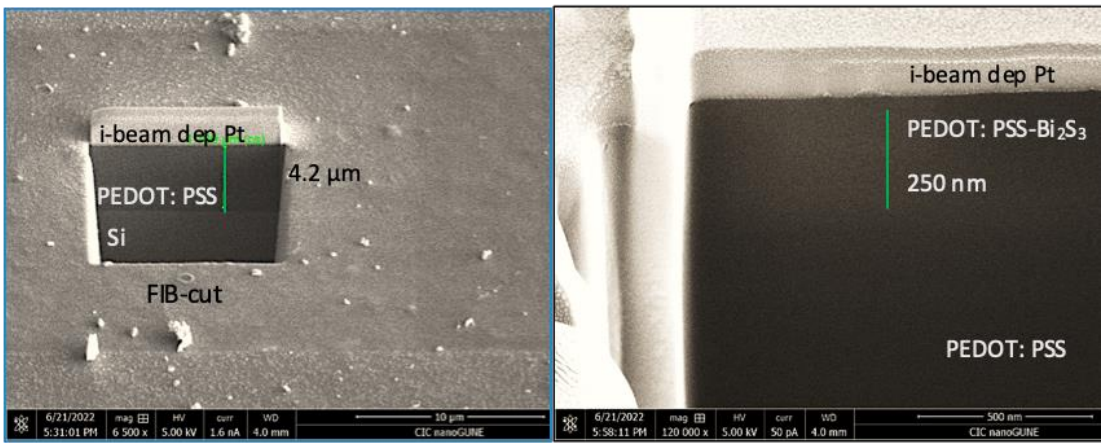

Figure 30. *SEM image of the cross-section of PEDOT:PSS after 800 cycles of Bi_2S_3 at 150 ^{0}C* ***(a)****, Expanded view of the cross-section* ***(b)****.*

4.4.4. Energy Disperse X-ray spectroscopy (EDX)

Energy-dispersive X-ray spectroscopy (EDX) was used to examine the composition of the ALD film grown at 150 °C on ZrO_2 NPs and on a lacey carbon TEM grid. Figure 31 shows the TEM image of the resulting Bi_2S_3 ALD coating and EDX elemental maps of the selected area for C, Zr, O, Bi and S. The EDX maps confirmed that Bi_2S_3 does not form continuous layers, neither on ZrO_2 NPs nor on the pure carbon substrates and shows an island-like growth, as explained in section 4.3.

Figure 31 also shows the EDX spectra of the Bi_2S_3 ALD coating, grown at 150 °C on ZrO_2 NP's. The quantitative EDX analysis showed that the Bi:S atomic ratio on the surface of the samples is 2:3, which agrees with the expected composition in Bi_2S_3. The copper signal originates from the copper TEM grid holder. The zirconia peak originates from the substrate.

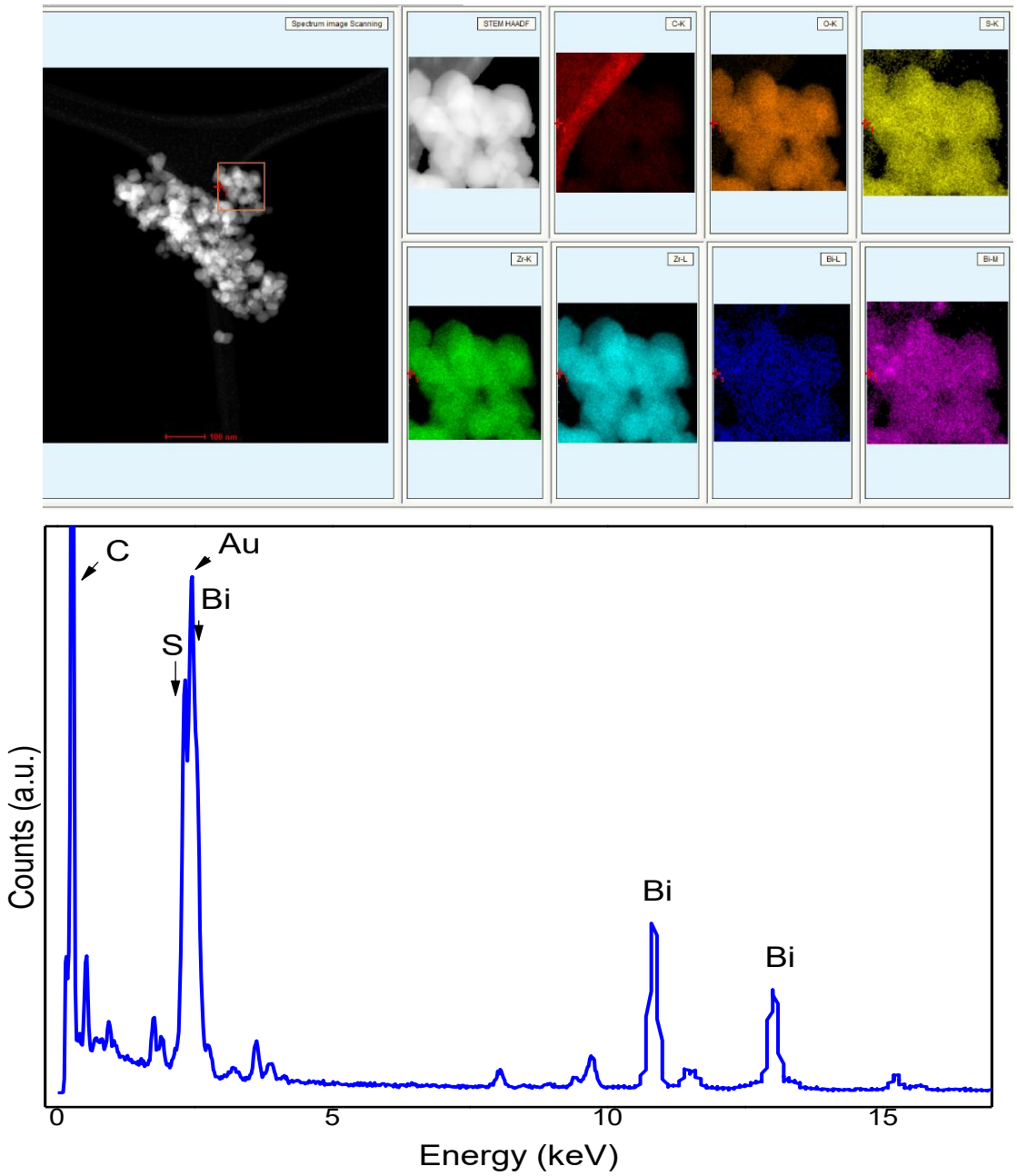

Figure 31. *TEM image of Bi_2S_3-coated ZrO_2 NPs on a lacey carbon TEM grid and elemental maps of the selected area for Zr, O, Bi and S and EDX spectrum of an Bi_2S_3 ALD coating, grown at 150 °C on ZrO_2 NPs.*

5. CONCLUSIONS

In this thesis the thin film growth characteristics of Bi_2S_3 from two precursors, $BiCl_3$ and H_2S, by ALD were studied. Afterwards, the synthesis of hybrid Bi_2S_3-polymer materials by VPI of $BiCl_3$ and H_2S, with PANI and PEDOT:PSS as polymeric substrates, was explored.

In-situ QCM studies of PANI and PEDOT:PSS upon single-precursor infiltration of TMA and H_2O and the Al_2O_3 VPI were performed. PEDOT: PSS showed a higher infiltration rate than PANI. This can be attributed to the larger number of groups that can react with TMA in PEDOT:PSS than in PANI. Also, the density of PEDOT:PSS is lower than the density of PANI, which can condition a better infiltration into and diffusion inside the polymer. (Figure 10, 11).

The *in-situ* QCM mass change vs. time during 10 VPI cycles, using H_2O and TMA at 110 ºC, with PEDOT: PSS as a substrate, is shown in figure 15. The TMA pulse leads to mass gain, while the H_2O dose leads to a slight mass decrease. Resulting from the Al_2O_3 VPI of PEDOT: PSS, the measured MGPC was 175 ng/cm^2. This is much higher than the typical ALD growth rate of Al_2O_3.

For the ALD of Bi_2S_3 using $BiCl_3$ and H_2S as precursors, the QCM data showed a linear and reproducible growth with the highest MGPC of 4 ng/cm^2 at 150^{o}C (Figure 20, 21). ALD of Bi_2S_3 showed an island-type of growth, forming crystalline, 10-15 nm sized particles instead of compact layers (Figure 27, 28). The EDX analysis showed that the Bi:S ratio on the surface was 2:3, indicating that the islands are formed by pure Bi_2S_3 (Figure 31). The TEM morphology analysis revealed the crystalline orientation of the grown Bi_2S_3.

The ATR-FTIR analysis of the infiltrated PANI and PEDOT:PSS showed the formation of new bonds in the polymeric structures as well as the presence of Bi-S bonds at the surface of the materials (Figure 25 and 26). These results prove the formation of stable hybrid materials. Unfortunately, the PANI samples became brittle after infiltration and couldn't be studied by electron microscopy.

The SEM images of the cross-section of PEDOT:PSS after 800 cycles of Bi_2S_3 VPI, processed at 150^{o}C, showed the formation of a hybrid layer that can be visualized as brighter subsurface area. It formed to the polymer depth of around 250 nm polymer of the total 4.2 µm thickness (Figure 30).

Hence, we demonstrated synthesis of a new stable PEDOT:PSS-Bi_2S_3 hybrid material by VPI using a moderate temperature (150^{o}C). The further experiments will focus on the TE performance of the fabricated materials and the optimization of the inorganic-polymer composition.

CONCLUSIONES

El objeto de estudio de esta tesis ha sido las características mostradas por el crecimiento de delgadas películas de Bi_2S_3 de $BiCl_3$ y H_2S mediante la técnica ALD. Posteriormente, se realizó la síntesis de materiales híbridos polímero-Bi_2S_3 mediante el VPI de $BiCl_3$ y H_2S en los polímeros PANI y PEDOT:PSS.

Se han realizado estudios de QCM *in-situ* de la infiltración de un solo precursor de PANI y PEDOT:PSS con TMA y H2O y VPI de Al_2O_3. Mostrando el polímero PEDOT: PSS una mayor tasa de infiltración que el polímero PANI. Este resultado puede ser la consecuencia de dos factores: un mayor número de grupos reactivos al TMA en PEDOT:PSS que en el polímero PANI o bien por la menor densidad del PEDOT:PSS respecto a la del PANI, pudiendo condicionar una mejor difusión e infiltración, respectivamente. (Figura 10, 11).

En la figura 15 se expone la variación de la masa QMC *in-situ* frente al tiempo a lo largo de 10 ciclos mediante la técnica VPI a 110 ºC pulsando H2O y TMA con PEDOT:PSS a modo de sustrato. Mientras que el pulso de TMA deriva en una ganancia de masa, la dosis de H_2O, conduce a una ligera disminución de la misma. El VPI de Al_2O_3 resultante de PEDOT: PSS MGPC es de 175 ng/cm^2, siendo ésta una cifra más elevada que la tasa de crecimiento que se da de Al_2O_3 utilizando la técnica ALD.

El cambio de masa QCM *in-situ* frente al tiempo durante 10 ciclos VPI utilizando H2O y TMA pulsando a 110 ºC con PEDOT: PSS como sustrato se expone en la figura 15. El pulso de TMA conduce a una ganancia de masa, mientras que la dosis de H_2O, de nuevo, conduce a una ligera disminución de la masa. El crecimiento de masa por ciclo (MGPC) de Al_2O_3 VPI resultante de PEDOT: PSS es de 175 ng/cm2. Siendo una cifra más elevada que la tasa de crecimiento de Al_2O_3 ALD.

Para el ALD de Bi2S3 utilizando $BiCl_3$ y H_2S, los datos de QCM indicaron un crecimiento lineal y reproducible con el mayor MGPC de 4 ng/cm2 a 150 ^oC (Figura 20, 21). Se observó un crecimiento de tipo isla en el cual se formaron partículas cristalinas de un tamaño de entre 10-15 nm en lugar de capas compactas (Figura 27, 28). Mediante el análisis EDX se mostró que la relación Bi:S en la superficie era de 2:3, lo que indica que las islas están formadas por Bi_2S_3 puro (Figura 31). El análisis morfológico TEM reveló la orientación cristalina del Bi_2S_3.

El análisis ATR-FTIR de los polímeros PANI y PEDOT:PSS infiltrados mostró la formación de nuevos enlaces en las estructuras poliméricas, así como la presencia de enlaces Bi-S en la superficie de los materiales (Figura 25 y 26). Estos resultados demuestran la formación de materiales híbridos estables. Lamentablemente, las muestras de PANI se volvieron frágiles después de la infiltración, resultando imposible el estudio por microscopía electrónica.

Una vez finalizados 800 ciclos de Bi_2S_3 mediante VPI procesados a una temperatura de 150 ºC, se obtuvieron las imágenes de la sección transversal del PEDOT:PSS mediante SEM, donde, de un espesor total de 4,2 µm se observa la formación de la capa híbrida a 250 nm, pudiendo ser esta visualizada como un área subsuperficial brillante (Figura 30).

Por consiguiente, se ha podido demostrar la síntesis de un nuevo material híbrido PEDOT:PSS-Bi_2S_3 estable mediante la técnica VPI a una temperatura moderada de 150 ºC.

Finalmente, se espera que el material híbrido resultante tenga un alto rendimiento TE.

6. BIBILIOGRAPHY

[1] B. Knopf, Y.H.H. Chen, E. de Cian, H. Förster, A. Kanudia, I. Karkatsouli, I. Keppo, T. Koljonen, K. Schumacher, D.P. van Vuuren, BEYOND 2020-STRATEGIES and COSTS for TRANSFORMING the EUROPEAN ENERGY SYSTEM, Clim Chang Econ (Singap). 4 (2013). https://doi.org/10.1142/S2010007813400010.

[2] J.S., T.D.G. Jadhao, Review on Exhaust Gas Heat Recovery for I.C. Engine, IJEIT. (2013) 93–100.

[3] W. Liu, X. Yan, G. Chen, Z. Ren, Recent advances in thermoelectric nanocomposites, Nano Energy. 1 (2012) 42–56. https://doi.org/10.1016/j.nanoen.2011.10.001.

[4] M. Famili, I.M. Grace, Q. Al-Galiby, H. Sadeghi, C.J. Lambert, Toward High Thermoelectric Performance of Thiophene and Ethylenedioxythiophene (EDOT) Molecular Wires, Adv Funct Mater. 28 (2018). https://doi.org/10.1002/adfm.201703135.

[5] H. Jin, J. Li, J. Iocozzia, X. Zeng, P.C. Wei, C. Yang, N. Li, Z. Liu, J.H. He, T. Zhu, J. Wang, Z. Lin, S. Wang, Hybrid Organic–Inorganic Thermoelectric Materials and Devices, Angewandte Chemie - International Edition. 58 (2019) 15206–15226. https://doi.org/10.1002/anie.201901106.

[6] H. Shirakawa, E.J. Louis, A.G. MacDiarmid, C.K. Chiang, A.J. Heeger, Synthesis of electrically conducting organic polymers: halogen derivatives of polyacetylene, (CH) x, J Chem Soc Chem Commun. (1977) 578. https://doi.org/10.1039/c39770000578.

[7] L. Wang, Z. Zhang, Y. Liu, B. Wang, L. Fang, J. Qiu, K. Zhang, S. Wang, Exceptional thermoelectric properties of flexible organic−inorganic hybrids with monodispersed and periodic nanophase, Nat Commun. 9 (2018) 3817. https://doi.org/10.1038/s41467-018-06251-9.

[8] Z. Fan, D. Du, X. Guan, J. Ouyang, Polymer films with ultrahigh thermoelectric properties arising from significant seebeck coefficient enhancement by ion accumulation on surface, Nano Energy. 51 (2018) 481–488. https://doi.org/10.1016/j.nanoen.2018.07.002.

[9] S.M. George, Atomic layer deposition: An overview, Chem Rev. 110 (2010) 111–131. https://doi.org/10.1021/cr900056b.

[10] I. Azpitarte, M. Knez, Vapor phase infiltration: from a bioinspired process to technologic application, a prospective review, MRS Commun. 8 (2018) 727–741. https://doi.org/10.1557/mrc.2018.126.

[11] T. Weckman, K. Laasonen, First principles study of the atomic layer deposition of alumina by TMA–H2O-process, Physical Chemistry Chemical Physics. 17 (2015) 17322–17334. https://doi.org/10.1039/C5CP01912E.

[12] M. Weber, A. Julbe, S.S. Kim, M. Bechelany, Atomic layer deposition (ALD) on inorganic or polymeric membranes, J Appl Phys. 126 (2019) 1–12. https://doi.org/10.1063/1.5103212.

[13] I. Azpitarte, G.A. Botta, C. Tollan, M. Knez, SCIP: a new simultaneous vapor phase coating and infiltration process for tougher and UV-resistant polymer fibers, RSC Adv. 10 (2020) 15976–15982. https://doi.org/10.1039/D0RA02073G.

[14] M.N. Rocklein, S.M. George, Temperature-induced apparent mass changes observed during quartz crystal microbalance measurements of atomic layer deposition, Anal Chem. 75 (2003) 4975–4982. https://doi.org/10.1021/ac030141u.

[15] S.A. Khan, S.B. Khan, L.U. Khan, A. Farooq, K. Akhtar, A.M. Asiri, Fourier transform infrared spectroscopy: Fundamentals and application in functional groups and nanomaterials characterization, in: Handbook of Materials Characterization, Springer International Publishing, 2018: pp. 317–344. https://doi.org/10.1007/978-3-319-92955-2_9.

[16] https://www.mt.com/mx/es/home/products/L1_AutochemProducts/ReactIR/attenuated-total-reflectance-atr.html, (n.d.).

[17] B.J. Inkson, Scanning Electron Microscopy (SEM) and Transmission Electron Microscopy (TEM) for Materials Characterization, in: Materials Characterization Using Nondestructive Evaluation (NDE) Methods, Elsevier Inc., 2016: pp. 17–43. https://doi.org/10.1016/B978-0-08-100040-3.00002-X.

[18] S. Turner, Structure, shape, defects and impurities in nanodiamonds investigated by HRTEM and STEM-EELS, in: Nanodiamonds, Elsevier, 2017: pp. 57–84. https://doi.org/10.1016/B978-0-32-343029-6.00003-9.

[19] N. Raval, R. Maheshwari, D. Kalyane, S.R. Youngren-Ortiz, M.B. Chougule, R.K. Tekade, Importance of physicochemical characterization of nanoparticles in pharmaceutical product development, in: Basic Fundamentals of Drug Delivery, Elsevier, 2018: pp. 369–400. https://doi.org/10.1016/B978-0-12-817909-3.00010-8.

[20] Weike Wang, Vapor Phase Infiltration (VPI) and Doping of Conducting Polymers, Universidad del País Vasco, 2017.

[21] https://www.sigmaaldrich.com/ES/es/product/aldrich/655201, (n.d.).

[22] O.P. Dimitriev, Doping of polyaniline by transition metal salts: effect of metal cation on the film morphology, Synth Met. 142 (2004) 299–303. https://doi.org/10.1016/j.synthmet.2003.10.003.

[23] K.S. Ryu, B.W. Moon, J. Joo, S.H. Chang, Characterization of highly conducting lithium salt doped polyaniline films prepared from polymer solution, Polymer (Guildf). 42 (2001) 9355–9360. https://doi.org/10.1016/S0032-3861(01)00522-5.

[24] V. Rajasekharan, T. Stalin, S. Viswanathan, P. Manisankar, Electrochemical Evaluation of Anticorrosive Performance of Organic Acid Doped Polyaniline Based Coatings, 2013. www.electrochemsci.org.

[25] N. Haddar, A. Kallel, J.-F. Pilard, P. Daniel, Synthesis and investigation of flexible conductive nanocomposite polyurethanes/polyaniline doped with NICL2, Polymer Bulletin. 79 (2022) 2523–2538. https://doi.org/10.1007/s00289-021-03647-4.

[26] I. Kulszewicz-Bajer, A. Proń, J. Abramowicz, C. Jeandey, J.-L. Oddou, J.W. Sobczak, Lewis Acid Doped Polyaniline: Preparation and Spectroscopic Characterization, Chemistry of Materials. 11 (1999) 552–556. https://doi.org/10.1021/cm980727a.

[27] G. Wypych, Handbook of polymers, n.d.

[28] https://www.sigmaaldrich.com/ES/es/product/aldrich/576379, (n.d.).

[29] S. Ranjitha, S. Vadivel, D.G. Rajarajan, J. Marimuthu, S. Natarajan, Structural and Optical Properties of Bismuth Sulfide Nanoparticles, n.d. www.ijsr.net.

[30] S.V.P. Vattikuti, J. Shim, C. Byon, Synthesis, characterization, and optical properties of visible light-driven Bi2S3 nanorod photocatalysts, Journal of Materials Science: Materials in Electronics. 28 (2017) 14282–14292. https://doi.org/10.1007/s10854-017-7287-6.

[31] J. Lee, W. Choi, Surface Modification of Sulfur Cathodes with PEDOT:PSS Conducting Polymer in Lithium-Sulfur Batteries, J Electrochem Soc. 162 (2015) A935–A939. https://doi.org/10.1149/2.0651506jes.

[32] Y. Liu, D. Sun, S. Askari, J. Patel, M. Macias-Montero, S. Mitra, R. Zhang, W.F. Lin, D. Mariotti, P. Maguire, Enhanced Dispersion of TiO2 Nanoparticles in a TiO2/PEDOT:PSS Hybrid

Nanocomposite via Plasma-Liquid Interactions, Sci Rep. 5 (2015). https://doi.org/10.1038/srep15765.

[33] E. Hosseini, V. Ozhukil Kollath, K. Karan, The key mechanism of conductivity in PEDOT:PSS thin films exposed by anomalous conduction behaviour upon solvent-doping and sulfuric acid post-treatment, J Mater Chem C Mater. 8 (2020) 3982–3990. https://doi.org/10.1039/C9TC06311K.

[34] A. Kellenberger, E. Dmitrieva, L. Dunsch, The stabilization of charged states at phenazine-like units in polyaniline under p-doping: an in situ ATR-FTIR spectroelectrochemical study, Physical Chemistry Chemical Physics. 13 (2011) 3411. https://doi.org/10.1039/c0cp01264e.

[35] X. Yang, Y. Wan, Y. Zheng, F. He, Z. Yu, J. Huang, H. Wang, Y.S. Ok, Y. Jiang, B. Gao, Surface functional groups of carbon-based adsorbents and their roles in the removal of heavy metals from aqueous solutions: A critical review, Chemical Engineering Journal. 366 (2019). https://doi.org/10.1016/j.cej.2019.02.119.

[36] K. Ashurbekova, K. Ashurbekova, I. Saric, E. Modin, M. Petravić, I. Abdulagatov, A. Abdulagatov, M. Knez, Molecular layer deposition of hybrid siloxane thin films by ring opening of cyclic trisiloxane (V3D3) and azasilane, Chemical Communications. 56 (2020) 8778–8781. https://doi.org/10.1039/d0cc04195e.